October 2018

Magma Envelopes, Enclaves and Rogue Crystals in the Atascosa Lookout Lava Flow: Magma Communication Across a Range of Crustal Levels

Christine Burrill

Magma Envelopes, Enclaves and Rogue Crystals in the Atascosa Lookout Lava Flow: Magma Communication Across a Range of Crustal Levels

A Thesis Presented

by

CHRISTINE M. BURRILL

Submitted to the Graduate School of the
University of Massachusetts Amherst in partial fulfillment
of the requirements for the degree of

MASTER OF SCIENCE

September 2018

Geosciences

Magma Envelopes, Enclaves and Rogue Crystals in the Atascosa Lookout Lava Flow: Magma Communication Across a Range of Crustal Levels

A Thesis Presented

by

CHRISTINE M. BURRILL

Approved as to style and content by:

_____
Sheila Seaman, Chair

_____
Michael Williams, Member

_____
Michael Jercinovic, Member

_____
Julie Brigham-Grette, Department Head
Geosciences

DEDICATION

To my grandmother, whose curiosity about the natural world continues to inspire me.

ACKNOWLEDGEMENTS

I would like to thank my advisor, Sheila Seaman, for her guidance, support and her uncanny sense of optimism. I would also like to thank Michael Williams for his incredibly useful comments and suggestions as well as Michael Jercinovic for being immensely helpful with the microprobe.

A special thanks to David Snoeyenbos for his thin sections and help with the microprobe, also Claire Pless for additional help with the microprobe and Marissa Minch for introducing me to the rock lab and thin section preparation. Thank you to Mike Rhodes for helping with the trace element analysis.

I wish to express my gratitude to the UMass Geosciences Department and Alumni for funding the research and covering travel expenses for the presentation of this project at the GSA meeting in California.

Last, but not least, a very heartfelt thanks to my grandfather, Kris and Alicia for encouragement and support. And my Aunt Janice who helped fund a lot of my education and travels – I cannot thank you enough.

ABSTRACT

MAGMA ENVELOPES, ENCLAVES AND ROGUE CRYSTALS IN THE ATASCOSA LOOKOUT LAVA FLOW: MAGMA COMMUNICATION ACROSS A RANGE OF CRUSTAL LEVELS

SEPTEMBER 2018

CHRISTINE M. BURRILL, B.A., MOUNT HOLYOKE COLLEGE

M.S., UNIVERSITY OF MASSACHUSETTS AMHERST
Directed by: Professor Sheila Seaman

The Atascosa Lookout lava flow is a mid-Tertiary trachyandesite flow that caps the rhyolitic to dacitic volcanic sequence exposed in the Atascosa Mountains of southern Arizona. The flow erupted near the beginning of extension in the southern Basin and Range following the floundering of the Farallon plate and during the development of the San Andreas fault. The flow hosts a variety of disequilibrium crystals and textures including resorbed and overgrown feldspar phenocrysts with inclusion-rich zones, quartz-bearing enclaves, and clusters of plagioclase +/- chromium diopside, magnesian augite, quartz, hornblende, and orthopyroxene crystals and envelopes of contrasting composition with both the groundmass and the enclaves.

Current evidence suggests that magma generation and differentiation commonly take place mainly in the lower crust and batches of magma are emplaced and equilibrate across a range of crustal levels. Crystallization depths and temperatures of various phases in the flow were obtained with new and revised geothermometers and geobarometers to examine the petrogenesis of the lava flow. Major elements of parental melts for most of the mineral phases were estimated using thermobarometry equilibrium tests and rare earth and trace element concentrations of parental melts of hornblendes and clinopyroxenes were calculated using known partition coefficients elements.

Thermobarometry shows distinct ranges of temperatures and pressures for each component of the flow and calculated parental melts of various phases are distinct from one another. Orthopyroxenes crystallized at depths greater than 25 km, at the highest temperatures from the most mafic parent, estimated to be a picro-basalt. Clinopyroxenes crystallized at 11.5 – 30 km, lower temperatures and a more evolved parent of basalt or trachybasalt composition. Plagioclase crystallized throughout the crust from a range of intermediate melts and hornblendes crystallized 12 – 13 km from a parental melt similar in composition to the groundmass. This study demonstrates the lava flow hosts minerals that crystallized from different parent melts at various crustal levels. Extension and previous magmatism provided a rapid path for magma to ascend, subduing crustal assimilation and enhancing the probability of a diverse crystal cargo that retains the record of the plumbing system beneath a volcanic complex.

TABLE OF CONTENTS

Page

LIST OF TABLES

LIST OF FIGURES

CHAPTER 1

INTRODUCTION

Products of volcanic eruptions are the petrologic probes into magma storage conditions and have been revealing increasing degrees of complexity in some systems as analytical abilities have improved (Cashman & Giordano, 2014). Earlier concepts of predominately liquid magma chambers that exist for extensive periods in the mid-shallow crust are being displaced by models of partially crystalline dikes and sills stacked throughout the crust that may be tapped in a single eruption (Cashman & Giordano, 2014; Annen et al., 2015; Karakas and Dufek, 2015; Putirka, 2017). These models are supported by studies showing evidence for mineral crystallization at a range of depths (Putirka, 1997; Geiger et al., 2016; Ubide & Kamber, 2018) and pluton construction through episodic growth of small magma batches over millions of years (Paterson et al., 2011; Annen et al., 2015). Also, seismic studies have failed to show large liquid magma bodies residing in the crust (Putirka, 2017).

Annen et al. (2006) proposed that mafic magmas fractionate mostly in the lower crust and that volcanic systems can produce less evolved lavas over time as the system is heated from long-term injection of hotter, more primitive magma. Tectonic processes, such as the extension of the crust, could lead to the interaction between more and less evolved melts stored at various levels of the crust producing hybrid magmas that may not be diagnosed through fractional crystallization trends alone (Annen et al, 2006). Modeling by Karakas and Dufek (2015) showed that over time, in extensional settings, the crustal component decreases with each successive emplacement of mantle-derived material and as crustal material is pushed away by extension. However, some models

show that open-system dynamics within a single magma reservoir can produce complex crystal zoning and fabrics and can bring together crystals that may have recorded very different physiochemical environments (Bergantz et al, 2015).

The Atascosa Lookout Lava Flow has a diverse crystal cargo characterized by disequilibrium textures and a bulk composition more mafic than the underlying rhyolitic volcanics. One key question is whether the lava flow represents the lower reaches of a single shallow, stratified magma chamber created though repeated injections and differentiation with minimal mixing. Or does the flow represent complex mixing in an open magma system as proposed in the Bergantz et al. (2015) model. Alternatively, the lava flow could represent magma that erupted from deeper in the crust and incorporated material from magma reservoirs at various depths within the crust.

To investigate the origin of the Atasacosa Lookout lava flow, storage and crystallization conditions of the various minerals were determined using new and revised thermometers and barometers. Similar crystallization pressures for the suite of minerals and diverse textural varieties of single minerals would be consistent with evolution in a single magma chamber in a limited range of crustal depth. Equilibrium melts were calculated as part of the thermobarometry calculations and these provide inside into whether minerals crystallized from similar or different magma compositions. Potential parental magmas were also calculated using measured trace and rare earth element compositions of minerals in diverse settings and published partition coefficients. These data were used to evaluate whether and to what degree these parental magmas were related. Some additional disequilibrium textural features were evaluated including radial pyroxene and zircon U-Pb dates were obtained to constrain how long it may have taken

for the lava flow to be assembled. All of the data are interpreted holistically in the broader context of the tectonics and thermal evolution of the crust to understand the more mafic character of the flow in relation to the underlying volcanic sequence.

CHAPTER 2

BACKGROUND

2.1 Magmatic Systems: Emplacement, Storage, Recharge, Triggering and Eruption

Understanding the emplacement of magma into the crust from the mantle and the conditions of storage and ascent of the magma and how these processes influence the eruption and compositions of volcanic products observed at the surface is a fundamental goal in volcanology. White et al. (2006) estimated the median ratio of volumes of magma that remain in the crust to magma that erupts at the surface to be about 5:1, indicating conditions in the crust are more favorable to the formation of plutons than facilitating eruptions. Even in volcanic arcs, that lie above continuous subduction and therefore a presumably steady magma-generating source, eruptions are episodic and plutonic-volcanic ratios are >30:1 (Paterson and Ducea, 2015). The density of magma relative to the surrounding crust strongly influences how far magma rises to the surface and commonly results in mafic magmas stalling in the lower crust at intercontinental settings while lithology and rheological boundaries can further slow or halt the ascent of magmas in the mid to upper crust (Cassidy et al., 2015). The tectonic setting (magnitude and orientation of principle stresses) can also influence the ability of magmas to erupt; transtensional tectonics generate faults that may provide pathways for magmas to reach the surface that might otherwise become trapped in the crust and differentiate or crystallize completely where compressional tectonics thicken the crust and inhibit magma from reaching the surface (Cassidy et al., 2015). A study at Mt. Etna (Armienti et al., 2013) suggested that water saturation has an important role of transporting magma

through the crust. Lack of water may also account for some magma stagnation in the crust (Putirka, 2017).

Recent studies suggest large plutons have been constructed incrementally from small pulses of magma over the course of hundreds to millions of years which complicate a seemingly well-established theory that eruptions are triggered by recharge of fresh magma into a magma chamber. These large plutons demonstrate that recharge alone may be an insufficient mechanism or at least demands that volcanologists provide more detail how recharge could be sufficient to trigger an eruption. Recharge and eruption triggering will vary depending on the magma model used to explain the formation and eruption of the Atascosa Lookout lava flow. Recent numerical simulations have shown that whether the magma erupts depends on the rate of emplacement and ability of smaller magma bodies to combine (Menard et al, 2011). During high rates of emplacement an eruption is likely to occur and drain the magma chamber(s) which speeds up cooling and solidification of the remaining magma left in the crust, while low rates of emplacement hinder the development of magma chambers and lead to cooling and solidification (Annen, 2009; Menard et al. 2011). Some combination of recharge and mixing could be sufficient to trigger an eruption (Putirka, 2017) which would rule out the formation of the Atascosa in a single, shallow stratified magma chamber.

It is possible for crystals with complex zoning to form in a decade or less which indicates that magmas may be able to mix and transition rapidly from a locked crystal mush to a mobile and eruptible fluid (Bergantz et al., 2015). If new magma is slowly injected into a reservoir from below, it will spread by porous media flow, but at higher injection velocities, more of the reservoir becomes fluidized, entraining crystals from

different parts of the reservoir that may have experienced different physiochemical environments, with little magma unmixed. Bergantz et al. (2015) plotted the trajectories and simulated compositional zoning of crystals in a single magma chamber that began adjacent to one another at the start of the simulation. The plot showed the crystals experienced distinct different chemical environments that were being mixed and resulted in complex zoning from a simple open system. Higher complexity would be expected from magmatic systems with large viscosity differences and multi-modal crystal populations (Bergantz et al., 2015).

2.2 The Atascosa Lookout Lava Flow

The Atascosa Formation is primarily composed of rhyolitic to rhyodacite ignimbrites and lava flows that are preserved in the Atascosa, Tumacacori Mountains and Cerro Colorado Mountains of southern Arizona (Fig. 1)(Webb and Coryell, 1954; Seaman et al., 1995). The Atascosa Lookout lava flow is the youngest, most compositionally

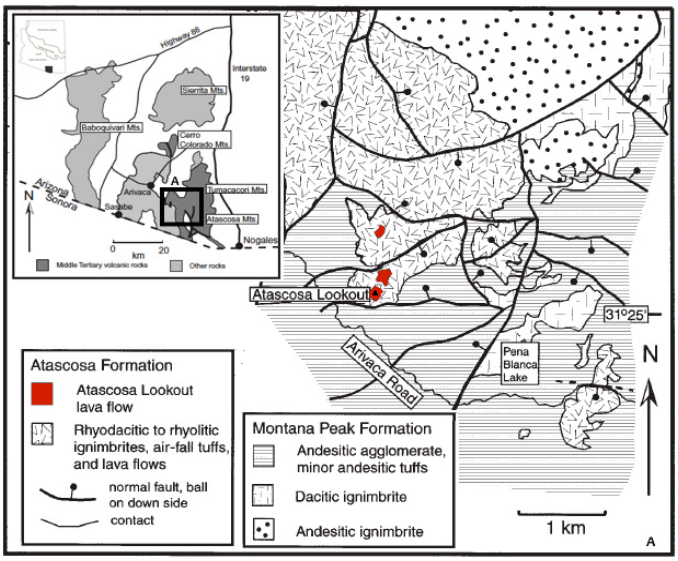

Figure.1 Location map of Atascosa Lookout lava flow, associated geologic formations and structures. Inset map shows location of Atascosa Mountains in southern Arizona and dark box indicates the zoomed in area of the larger map. Exposures of the lava flow are filled in red and underlying units of the Atascosa Formation are outlined with the V-pattern. (modified from Seaman 2000).

primitive unit of the Atascosa Formation and is limited to three exposures in the Atascosa Mountains (Seaman, 2000). The Atascosa Lookout lava flow is a trachyandesite on the basis of whole-rock analyses, but the groundmass is trachydacite (Seaman, 2000). Crystal clusters, plagioclase glomerocrysts, magmatic enclaves and phenocrysts of plagioclase and hornblende make up ~ 20% of the lava flow (Seaman, 2000). Magma envelopes, which are aphyric, chilled magma of contrasting color and composition to the groundmass, surround some of the crystal clusters, plagioclase glomerocrysts and enclaves (Fig. 2) (Seaman, 2000).

2.2.1 Volcanic Stratigraphy

The Atascosa, Tumacacori and Cerro Colorado Mountains form a volcanic complex along the southern Arizona border that is 27.7 Ma - 23.3 Ma years old ($^{40}Ar/^{39}Ar$ dates; Seaman et al., 1995) and are composed of thick sequences of andesitic to rhyolitic rocks that belong to the Atascosa or Montana Peak Formations (Seaman, 2000). The Atascosa and Tumacacori Mountains are nearly contiguous, separated by a structurally complex valley but have compositionally and texturally distinct units resulting from episodic eruptions (Seaman, 2000). Volcanism began around 26 Ma in the Cerro Colorado Mountains and 25.5 Ma in the Tumacacori Mountains and is mostly preserved in the 800-foot-thick Atascosa Formation that is tilted and fractured (Nelson, 1963; Seaman, 2000).

The Atascosa Formation is separated from the older Montana Peak Formation by an angular unconformity and petrified wood can be found at the contact, suggesting the presence of a forest on the erosional surface (Nelson, 1963). The Montana Peak Formation consists of andesitic and dacitic ignimbrites and lava flows. $^{40}Ar/^{39}Ar$ dating of

hornblende from the uppermost part of the formation provides an age of 27.7 Ma (Seaman, 2000). Lying unconformably below the Montana Peak Formation is the Cretaceous Oro Blanco member of the sedimentary Bisbee Formation and the Parajito Lavas (Nelson, 1963; Seaman, 2000).

2.2.2 Tectonic Setting

The Atascosa Lookout lava flow is located in the Southern Basin and Range, and in a state that has seen at least six major episodes of volcanism (Reynolds et al., 1986). Much of the continental crust that underlies Arizona formed between 1.8 and 1.6 Ga from collisions of volcanic arcs and associated sedimentary rocks, later metamorphosed to amphibolite facies and intruded by large granite plutons (Reynolds et al., 1986). Sparse volcanism occurred from 1.2 to 1.1 Ga and was then mostly absent for about a billion years while the area was intermittently flooded by shallow seas (Reynolds et al., 1986). In the Jurassic (200-145 Ma), volcanism became widespread as a northwest trending volcanic arc crossed southern Arizona and the Farallon plate subducted eastward beneath North America transforming the entire western edge of North America into a convergent plate boundary (Reynolds et al., 1986, Sonder and Jones, 1999).

The subduction of the Farallon plate became increasingly shallow between 60 and 40 Ma and magmatism migrated east with the shallowing of the subducting slab (Sonder & Jones, 1999; Ward, 1991; Copeland et al., 2017). Around 40 Ma, the angle of the subducting slab increased and magmatism migrated back west followed by slab breakoff and/or rollback (Copeland et al., 2017). Widespread volcanism associated with extension occurred across the western United States, largely during the mid-Tertiary time (37-15

Ma) (Sonder and Jones, 1999; Ward, 1991). The main period of ash flow volcanism occurred between 40-25 Ma in the Great Basin, southern Arizona and New Mexico followed by a change to bimodal, mainly basalt eruptions (Armstrong and Ward, 199; Christiansen and Lipman, 1972).

This change in volcanism coincided with the merging of the Arizona and Nevada magmatic fields around 25-22 Ma and the reorientation of stress patterns across the western U.S as the tectonic setting changed (Armstrong and Ward, 1991). The development of the San Andreas fault system occurred between 27 and 16 Ma. The plate boundary to the west of the Southern Basin and Range experienced a combination of slow subduction and strike-slip motion and eventually became a right-lateral transform fault as the spreading ridge separating the Pacific and North American plates was subducted and the two plates came into contact (Atwater 1970; Sonders and Jones, 1999). The Atascosa-Tumacacori-Cerro Colorado (ATCC) volcanic complex is related to this transition from convergent orogenesis to back-arc extension (Christiansen & Lipman, 1972; Elston, 1984; Gans et al., 1989; Leeman & Fitton 1989; Lipman & Glazner, 1991).

According to the linear equation of Putirka and Platt (2012), when using 31.42 degrees latitude for the Atascosa Lookout Lava Flow, extension would have begun in this part of Arizona around 31.9 Ma. The volcanism in the ATCC began just before the detachment phase of the metamorphic core complex development in the Baboquivari Mountains to the west (Goodwin and Haxel, 1990; Seaman, 2000). Metamorphic core complexes are exposures of ductilely deformed middle crust that are a result of extension and, in the southwest U.S., followed the large, voluminous intermediate composition

magmatic fields, suggesting a close relationship between magmatism and extension that produces these core complexes (Parsons, 1995).

The mid-Tertiary volcanic rocks in the ATCC share similar geochemistry and stratigraphy to many Cenozoic volcanic fields in western Mexico, southwestern New Mexico and Arizona. The sequence of volcanic rocks in southwestern Arizona typically start with a thin sequence of mafic to intermediate lava flows followed by voluminous felsic lava flows and pyroclastic rocks interbedded with some intermediate to mafic lava flows (Spencer et al., 1995). The sequence is then topped off with basaltic andesite flows, which Cameron et al. (1989) called the Southern Cordilleran Basaltic Andesite Suite (SCORBA). These flows have trace-element and isotopic signatures of orogenic (arc) rocks and 52-57% SiO_2 and are hypothesized to have erupted in a more extensional environment than the preceding intermediate-silicic rocks (Cameron et al., 1989). This allowed them to reach the surface more quickly and directly, undergoing less differentiation (Cameron et al., 1989). The Atascosa Formation follows the regional general stratigraphic pattern with the Atascosa Lookout Lava flow being of similar age, stratigraphic position and composition to the SCORBA.

The tectonic history may be important for understanding the petrogenesis of individual events, such as the Atascosa Lookout lava flow, by understanding the prevailing crustal conditions. Although the Southern Basin and Range has been less volcanically active for the last 10-15 m.y. there is currently anomalously high heat flow (80 -100 mW m^{-2}) attributed to upflow of hot material during extension in the Cenozoic (Lachenbruch & Sass, 1977; Lachenbruch et al., 1994). Thermobarometry of xenoliths from around the state (e.g. McGuire, 1994) also suggest an elevated geotherm and

geothermal studies indicate a present geothermal gradient in excess of 50 ºC/km (Giardina & Conley, 1978). Seismic studies show the current thickness of crust in southern Arizona to be ~25 km with a relatively thin crust-mantle transition zone, made smooth - in terms of seismic velocities changes - by mafic intrusions (Goodwin & McCarthy, 1990; Humphreys & Dueker, 1994; McGuire, 1994). Therefore, magma producing the Atascosa Lookout lava flow over 23 Ma would have emplaced into hotter and slightly thicker crust than present when volcanic activity was higher and before extension had thinned out the crust.

2.2.3 Petrography

Detailed petrography of the Atascosa Lookout lava flow was performed by Seaman (2000) and her work is summarized here to establish a potential relationship between textures and thermobarometry results later. The main components of the flow are the groundmass, the crystal clusters, enclaves, the large textural variety of plagioclase, the chromium clinopyroxene and the hornblende crystals with dark reaction rims. These components, based on the petrography alone, are suggestive of mixing of several distinct magmas.

The groundmass of the Atascosa Lookout lava flow consists of brown glass and micron-sized plagioclase crystals. Areas more gray in color with small hematite crystals are swirled in the groundmass and are slightly devitrified glass of contrasting composition compared to the more abundant brown glass (Seaman, 2000). Fine-grained, wispy, gray-brown material, referred to as magma envelopes, surrounds many crystal

clusters, enclaves and plagioclase glomerocrysts. These magma envelopes have high K, MG and low Si relative to the groundmass (Seaman, 2000).

Crystal clusters, less than 1 mm to ~1 cm in diameter occur throughout the lava flow and typically contain quartz, clinopyroxene, orthopyroxene, plagioclase and/or hornblende crystals that protrude into the groundmass. This suggests that these crystal clusters were loose aggregates, rather than xenoliths, when they entered the host magma (Seaman, 2000). Plagioclase occurs in nearly all clusters and the combination of quartz and chromium diopside or orthopyroxene is common (Seaman, 2000).

Enclaves are 0.5-2.0 cm in diameter and droplet shaped with smooth edges. The enclaves consist of plagioclase (~45%), quartz (~25%), illmenite (~15%) and vesicles (~15%) and are relatively coarser than the groundmass (Seaman, 2000). Although enclaves are quartz-bearing, they have 3-5 wt.% less SiO_2 and ~3 wt.% less total alkalis than the surrounding groundmass glass. The shape, composition and coarse-grained texture suggest that the enclaves are

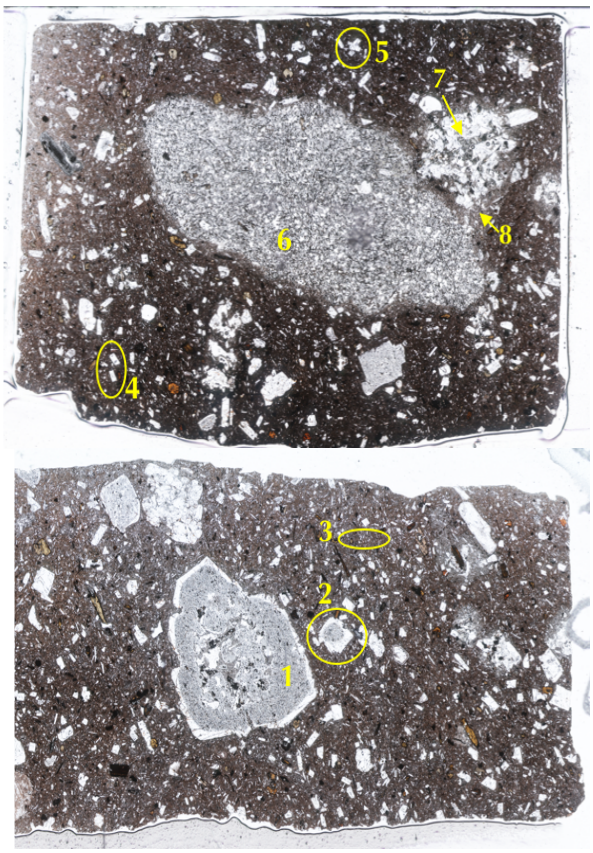

Figure 2. Thin sections showing the components of the Atascosa Lookout lava flow. (1) Large honeycomb plagioclase, (2) Dusty plagioclase, (3) Plagioclase laths, (4) Clear plagioclase (no inclusions), (5) Plagioclase glomerocrysts (honeycomb), (6) Course-grain quartz-bearing enclaves, (7) Crystal clusters (Plag ± Qtz, Hbld, Opx, Mg-Augite, Cr-diopside), (8) Magma envelopes (+K & Mg –Si)

magmatic droplets that crystallized relatively slowly in the present host to have allowed for larger crystals (Seaman, 2000).

Plagioclase crystals appear with honeycomb and dusty textures along with melt inclusions, as clear phenocrysts with no inclusions, plagioclase laths and glomerocrysts (aggregate of plagioclase crystals). Generally, the honeycomb plagioclase form the glomerocrysts and large melt inclusions are found in the interiors. Their rims are inclusionless and are higher in calcium than their interior zones. Dusty plagioclase crystals have the opposite character, with higher-calcium interiors that grade to a lower-calcium rim. Clear plagioclase phenocrysts rarely have zoning or reabsorption but in crystal clusters they show high-calcium cores that grade to thin low-calcium rims. The clear phenocrysts may have grown in the same magma after the dusty and honeycomb plagioclase or in a different magma altogether (Seaman, 2000).

The chromium concentration of some clinopyroxene crystals reaches 0.8 wt % Cr_2O_3 and is associated with higher Al and Mg concentrations (Seaman, 2000). The chromium clinopyroxene and orthopyroxene crystals are the most compositionally primitive crystals in the lava flow and have only been identified in the crystal clusters (Seaman, 2000). Their presence in this trachyandesitic flow makes them a particular interesting target for thermobarometry.

Hornblende is the abundant ferromagnesian phase of the groundmass. Seaman (2000) observed that the hornblende crystals have rounded margins, thick black rims and show no variation in appearance or composition in their occurrence in the groundmass or crystal clusters. Electron microprobe analysis of the rims showed that they were lower in Si, Mg, Ca and K and higher in Al and Fe than fresh hornblende.

2.2.4 Strontium Isotopic Data

Even though petrography performed by Seaman (2000) suggest distinctly different origins for many of the components of the flow, strontium isotopic ratios for plagioclase glomerocrysts, chromium clinopyroxene in crystal clusters, groundmass, enclaves, and magma envelopes, measured by Seaman (2000), were found to be similar enough that a broad genetic relationship is possible between all of these materials. Differences in the initial ratios could be explained by a small amount of crustal assimilation of Jurassic and Proterozoic plutonic country rocks (Seaman, 2000). The groundmass, one of the most evolved components of the flow, has the highest initial $^{87}Sr/^{86}Sr$ ratio of 0.707866-0.707899 (Seaman, 2000). The cores of the plagioclase glomerocrysts have a higher $^{87}Sr/^{86}Sr$ ratio than their rims but have values similar to a core of an enclave. Glomerocrysts rims, clinopyroxene crystals and magma envelopes have similar initial $^{87}Sr/^{86}Sr$ ratios (0.7076), but the ratios of clinopyroxenes are slightly lower.

2.2.5 Previous Thermobarometry

Plagioclase and hornblende frequently occur as euhedral crystals in the groundmass and in crystal clusters of the Atascosa Lookout lava flow. The amphibole–plagioclase thermometer (Holland and Blundy, 1994) was used by Seaman (2000) to obtain crystallization temperatures of the groundmass and crystal clusters for the Atascosa Lookout lava flow. The average temperature calculated for the groundmass was 801°C and for the crystal clusters was 838°C.

CHAPTER 3

METHODS

3.1 Samples

Samples from the Atascosa Lookout Lava Flow were collected by Sheila Seaman in the 1990s from Atascosa Lookout and Atascosa Peak. Thin sections that were made for the initial petrologic and geochemical study published in 2000 were re-polished and carbon coated for this study. Two additional thin sections were made in-house by David Snoeyenbos.

3.2 Scanning Electron Microscopy

Back-scattered electron (BSE) images were collected with the Zeiss EVO50 variable pressure Scanning Electron Microscope (SEM) at the University of Massachusetts Amherst in order to document the variety of textures in the phenocrysts more thoroughly. The two new thin sections prepared by David Snoeyenbos were used specifically because each thin section contained an usual round ball of chromium clinopyroxene that was visible in hand sample and not observed in the previous thin sections. Thin sections were imaged under high vacuum with a carbon coat.

3.3 Electron Probe Microanalysis (EPMA)

Microanalysis of minerals was performed on the Cameca SX50 at the University of Massachusetts Amherst under the direction of Michael Jercinovic. The microprobe is equipped with five wavelength-dispersive spectrometers for quantitative analysis and a PGT-IMIX energy-dispersive spectrometer for rapid qualitative analysis. Quantitative analyses were performed on hornblende and clinopyroxene crystals in different hosts to

obtain compositional information for thermobarometry calculations. Full thin section mapping was performed on a section that contained a large crystal cluster, clearly visible to the naked eye, followed by mapping of single crystals. Compositional maps of Si, Mg, K, Fe, Cr, Al and Ti were generated and quantitative analyses were performed on transects of clinopyroxenes in the groundmass and orthopyroxenes in crystal clusters. Traverses across a clinopyroxene and multiple orthopyroxene crystals were used to analyze their growth conditions and composition in detail.

3.4 Laser Ablation Inductively Coupled Mass Spectrometry (LA-ICP-MS)

Minerals in standard thin sections were analyzed for trace elements using a Nu instruments AttoM® high resolution laser ablation inductively coupled plasma mass spectrometer at the University of New Hampshire's Plasma Geochemistry Lab under the direction of Julie Byrce and Florencia Fahnstock. Hornblende, clinopyroxene and plagioclase were analyzed with a Photon Machines Excite 193 nm Excimer laser to obtain trace element compositions. NIST 612 was used for instrument calibration. A basalt glass ML3B-G was used as the primary standard. Four standards were analyzed before and after each run and one standard was used in between 10-12 individual analyses. Laser settings include a beam size of 40 μm and repetition rate of 4 Hz. Analyses were performed over three sessions with four thin sections loaded in the instrument per session. Data was processed using Iolite software which normalizes to Ca.

Trace element abundances were plotted in spider diagrams normalized to primitive melt using ratios of McDonough and Sun (1995). The purpose of the plot is to see if the pattern of elements is different between the same mineral analyzed in different settings of the lava flow (groundmass, enclaves, clusters and magma envelopes). Different trace

element abundances would be expected if the minerals came from different magma batches that evolved separately at different depths in the crust. The overall shape of the REE patterns and the individual anomalies were also evaluated in order to understand the generation and evolution of the parental melt.

3.5 Thermobarometry

Temperature is a fundamental parameter that effects the rheological behavior and crystallization history of a magma and the partial melting conditions of the source rock and two-phase thermometers have been widely used to constrain the crystallization temperature of volcanic rocks (Putirka, 2008; Siegel et al., 2017). However, Blundy and Cashman (2008) showed that when applied to experimental phases, two-phase thermometers can under- or overestimate temperature up to 300 °C (Ridolfi et al. 2010). Calibration is based on two or more phases being in equilibrium, so these geothermobarometers are not suitable for hybrid and variously re-homogenized magmas (Ridolfi et al. 2010).

New and revised 'glass' (liquid) and single-crystal thermobarometers have expanded the ability to extract information from complex volcanic rocks hosting minerals in disequilibrium (Putirka, 2008; Ridolfi et al. 2010). Larger experimental data sets and empirical corrections for non-ideal behavior have provided useful constraints for calibration (Nimis & Taylor, 2000). These new models were used to obtain the pressure and temperature conditions of the Atascosa magmatic system. Pressures were converted to depths by using a density of 2.8 g/cm^3 for the lithosphere beneath the volcano.

3.5.1 Clinopyroxene Thermobarometry

Thermobarometric calculations for clinopyroxene crystals in the groundmass and clusters were performed using the iterative algorithms in the supplemental materials of Putirka (2008). Both pressure-dependent and independent thermometers and temperature-dependent and independent barometers based on clinopyroxene compositions and clinopyroxene-melt equilibrium were used in these calculations.

The compositions of the enclaves, magma envelopes and groundmass were tested as nominal equilibrium melts and when those failed equilibrium tests, compositions of the melt were estimated using the same equilibrium tests. One test is to compare the observed and predicted values for Fe-Mg exchange to 0.27, but if Fe^{3+} is significant, the value should be between 0.27 and 1. The second test is to see if the calculated value for $K_D(Fe\text{-}Mg)^{cpx\text{-}liq}$ is equal to 0.27 ± 0.03 and the third test is to evaluate the observed and predicted components using the equilibrium graph. Data that lie close to the one-to-one line (within 10%) are accepted for the thermobarometric calculations. A final test is to evaluate whether the calculated crystallization temperatures are less than calculated saturation temperatures.

3.5.2 Orthopyroxene Thermobarometry

New thermometers developed by Putirka (2008) based on orthopyroxene-liquid equilibria have applicability to T=750-1600 C, P = 0-11 GPa, SiO_2 = 33-77 wt.% and H_2O = 0-14.2 wt.%. One thermometer (Equation 28b, p. 85) uses only liquid components to determine the temperature of orthopyroxene saturation and is based on a global non-linear regression while the other (Equation 28a, p. 85) was tested and calibrated using experimental data with cation sums between 3.7 and 4.03 (Putirka, 2008). Two

barometers (Equation 29a and 29b, p. 87) use orthopyroxene and liquid components and the third (Equation 29c, p. 87) uses orthopyroxene components only. All three barometers are temperature dependent and both thermometers are pressure dependent, therefore calculations are solved by iteration in the spreadsheet. An equilibrium liquid was determined by modification of the liquid by Elkins et al. (2000) and checking for equilibrium by comparing calculated values for K_D (Fe-Mg) = 0.29±0.06 and the Rhodes's diagram which graphically shows the equilibrium between the orthopyroxene and the melt by plotting 100xMg# of the liquid vs. 100xMg# of orthopyroxene (Putirka, 2008). On the diagram there is a line with envelopes represents the KD (Fe-Mg) = 0.29±0.06 and a melt is acceptable when the data plot within these envelopes (Appendix B).

3.5.3 Hornblende Thermobarometry

The Al-in-hornblende barometers of Johnson & Rutherford (1989), Hammarstrom & Zen (1986), Schmidt (1992) and Anderson & Smith (1995) require certain mineral assemblages to be present with hornblende. However many igneous systems, including the Atascosa Lookout lava flow, lack these equilibrium mineral assemblages. Therefore we use the single-crystal thermobarometer (AMP-TB.xls) of Ridofli et al. (2010) to calculate the physical–chemical conditions of hornblende crystallization in the groundmass, crystal clusters and magma envelopes. The amphiboles of the lava flow have dehydration or reaction rims but they retain inner zones with homogeneous composition that can be used for thermobarometry. Ridolfi et al. (2010) found a good match between the results obtained with the new single-crystal model and many other

suitable thermobarometric constraints for several well-known calc-alkaline volcanoes (e.g. Mount St Helens, Redoubt and Soufriere Hills).

3.5.4 Plagioclase-melt Thermobarometry

Mineral-melt pairs were selected for the Putirka (2008) thermobarometer through the equilibrium test based on An-Ab exchange. Pressure and temperature calculations are accepted for melts that fall within the interval $KD_{(Ab-An)} = 0.1 \pm 0.05$ for $T<1050^{o}C$ and $KD_{(Ab-An)} = 0.27 \pm 0.11$ for $T>1050^{o}C$. The nominal melts provided in the spreadsheet from the supplementary materials of Putirka (2008) and the groundmass, enclave and magma envelope compositions were tested for each plagioclase crystal.

3.5.5 Zircon Saturation Thermometry

There are four models to calculate zircon saturation temperature: Watson and Harrison (1983), Hanchar and Watson (2003), Boehnke et al. (2013) and Gervasoni et al. (2016). The zircon saturation thermometer, initially formulated by Watson and Harrison (1983), provides estimates of the temperature when zircon begins crystallizing in a cooling magma and has been used to interpret the peak temperatures that magmatic rocks experienced and estimate partial melting temperatures (Siégel et al., 2017). The silica content of the melt controls the compositional parameter, M ((Na+K+2*Ca)/(Al*Si)), which dictates the saturation levels for zircon crystallization (Watson & Harrison, 1983).

Boehnke et al. (2013) refined the original Watson and Harrison (1983) model by re-analyzing the original experimental run products of Watson and Harrison (1983) with a modern electron microprobe along with new experiments of their own. Both models of Watson and Harrison (1983) and Boehnke et al. (2013) are widely accepted and work

well in mostly aluminous melt compositions between $1.3 \leq M \leq 2$ but less information exists on whether these models can be used with melt compositions outside the calibrated range of melts or at higher temperatures (Gervasoni et al., 2016).

Gervasoni et al. (2016) performed zircon crystallization experiments in a range of compositions at high temperatures, extending the original model proposed by Watson and Harrison (1983) and Boehnke et al. (2013). The new compositional parameter G (3 · Al2O3 + SiO2)/(Na2O + K2O + CaO + MgO + FeO), calculated from molar proportions of electron microprobe data, allows their model to be applied in all intermediate to felsic melts from peraluminous to peralkaline compositions (Gervasoni et al., 2016).

Major element analyses and the Zr concentration of whole rock and groundmass composition of the lava flow from Seaman (2000) were used as input for these models and the average Zr concentration of the three whole rock measurements were used for the groundmass calculations. Then a range of Zr concentrations were tested with the groundmass to find the upper and lower limits of crystallization. The compositional parameters were assessed to choose which model give the most likely zircon saturation temperature for the Atascosa Lookout lava flow.

3.6. Zircon U-Pb Ages

Spot analyses of four zircon grains in thin section ATXC3B were performed at the Arizona Laserchron Center at the University of Arizona using the Thermo Scientific Element2 ICPMS. The Element2 is able to determine individual zircon U-Th-Pb ages with ~2-3% (2-sigma) precision. The standards that were used include Fish Canyon Tuff (28.50 ± 0.4 Ma), R33 (419 ± 0.4 Ma) and an in-house standard Sri Lanka zircon (563.5 ± 2.3 Ma) Before analysis, the zircon are imaged with a Hitachi 3400N SEM equipped

with a Gatan ChromaCL2 detector. Cathodoluminescence (CL) images are created for each sample to identify complexities such as inheritance or overgrowths and ensure that analyses are performed on homogenous areas of crystals.

3.7. Calculation of Parental Magmas

Partition coefficients (K_D) for trace elements in hornblende and clinopyroxene were obtained from the online GERM (Geochemical Earth Reference Model) database. Partition coefficients vary with temperature, pressure and composition of the melt and the latter commonly has the largest effect on the value. For example, K_D values can differ by up to one or two orders of magnitude for basalts and rhyolites (Winter 2010). Therefore, equilibrium liquids estimated from the thermobarometry calculations were used as a guide for which K_D values to choose. Hauri et al. (1994) calculated partition coefficients for clinopyroxene using a basaltic composition and Luhr et al. (1984) used trachyandesite for the hornblende. A study using a low-silica rhyolite for the hornblende partition coefficients, which would be a composition closer to the groundmass was considered, but a very limited number of partition coefficients were calculated and were not significantly different than some of the partition coefficients for the trachyandesite.

The trace element abundances of the estimated equilibrium melts (C_L) were obtained with the equation for the partition coefficient $K_D = C_S / C_L$ and then plotted on a multielement diagram and compared to the groundmass, enclaves and magma envelopes.

CHAPTER 4

RESULTS

4.1 Petrography and Textural Analysis

The back-scattered electron (BSE) images obtained with the scanning electron microscope (SEM) of two new thin sections show a variety of textures. Three isolated chromium clinopyroxene clusters with usual radiate textures similar to spherulites were observed with varying size, shape and radiate texture development. The first semi-spherical clinopyroxene is ~3.5 mm in diameter and has intergrowth of another mineral (Fig. 3a). The spherical clinopyroxene is ~100 μm and has fibrous texture (Fig. 3b) and is surrounded by a cloud of anhedral minerals. The third clinopyroxene is ~300 μm in diameter but does not have well defined interior texture and appears to have been extensively broken down (Fig. 3c). There appears to be pieces of hornblende and abundant oxides within the clinopyroxene.

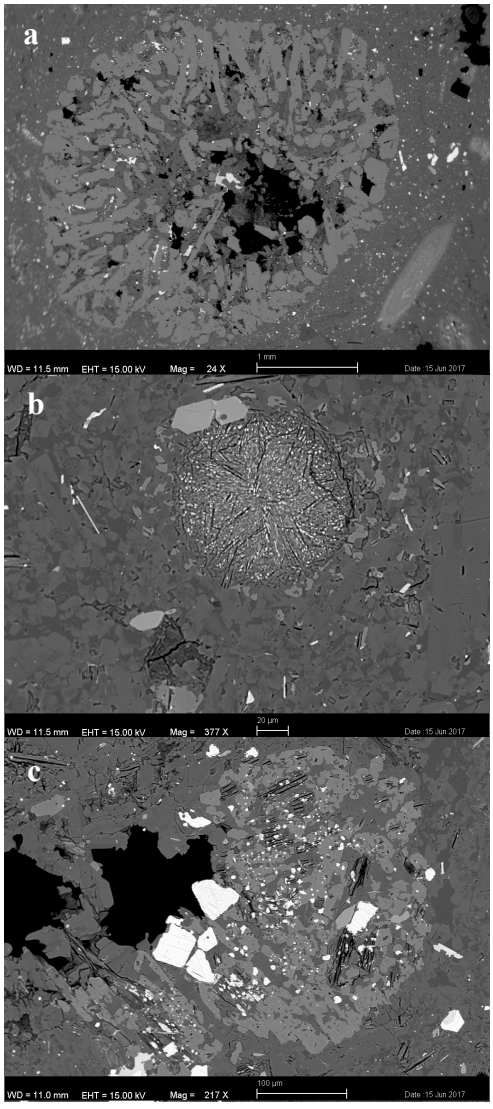

Figure 3. Backscatter electron images of chromium clinopyroxene with radiate texture.

A variety of textures observed in other components is show in Figure 4. Corroded or resorption features such as skeletal or branching texture (Fig. 4a) and embayed crystals such as the

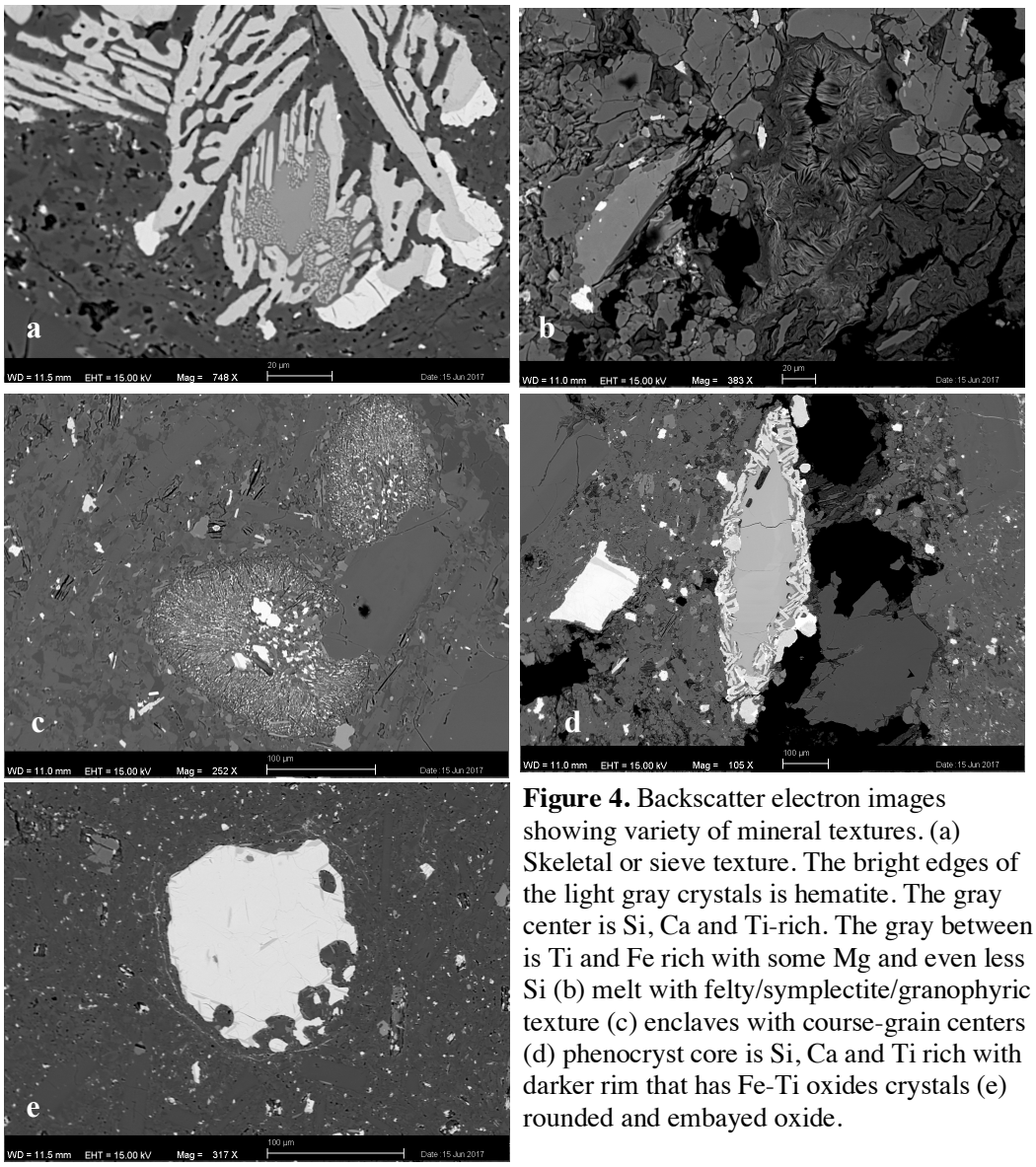

Figure 4. Backscatter electron images showing variety of mineral textures. (a) Skeletal or sieve texture. The bright edges of the light gray crystals is hematite. The gray center is Si, Ca and Ti-rich. The gray between is Ti and Fe rich with some Mg and even less Si (b) melt with felty/symplectite/granophyric texture (c) enclaves with course-grain centers (d) phenocryst core is Si, Ca and Ti rich with darker rim that has Fe-Ti oxides crystals (e) rounded and embayed oxide.

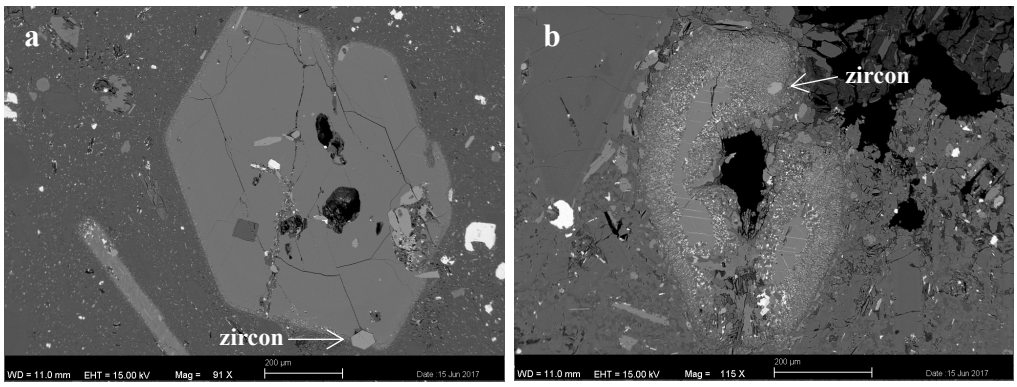

Figure 5. Backscatter electron images of hornblende showing the range of development of reaction rims. Euhedral hornblende crystal with a thin reaction rim (a) and a hornblende with rounded edges and thick reaction rim (b). Zircons occur frequently in close proximity or included in hornblendes.

oxide shown in Figure 4e. Enclaves, globs of magma with a different temperature and composition than their host, are present with course-grained interiors and clouds of crystals surrounding the outside. Recrystallization of crystal in reaction rims (Fig. 4d) and melt with a felty texture (Fig. 4b) are possible indicators of magma mixing.

Hornblende occurs with a range of sizes of reaction rims present and two end members are shown in Figure 5. Euhedral to semi-euhedral crystals of hornblende have thin reaction rims (10-20 μm) while other hornblende crystals have been almost entirely converted to the reaction rim material (~100 μm). An abundance of small zircon are present in the groundmass and in the different components of the lava flow, particularly in hornblende (Fig. 5). Zircon were not documented or discussed in previous studies of the lava flow and present a new avenue of probing the magma plumbing system.

4.1.1 Clinopyroxene & Orthopyroxene Zoning

Clinopyroxene and orthopyroxene crystals appear Fe-, Mg-, and Cr-rich and orthopyroxenes are Ca-poor relative to clinopyroxenes in full thin section maps. Maps of single clinopyroxene crystals in the groundmass showed coarse zoning in Cr, Al and Ti (Fig. 6). One crystal is orientated perpendicular to the c-axis and shows the zoning very clearly. The core has a thin band of high Cr that defines its boundary, followed by a wide Cr-poor zone that sharply turns to a relatively thinner Cr-rich zone that gradually fades into a wide Cr-poor zone which is followed by the outside rim of the crystal which is Cr-rich (Fig. 6). Chromium reaches 0.19 wt % in the core, 0.26 wt% in the inner zone and 0.11 wt% at the rim. There are also zones of relatively higher aluminum and titanium that are anticorrelated with chromium. The zoning of all three elements mirrors the euhedral faces of the crystal. The compositional changes occur in a step-zoning fashion with

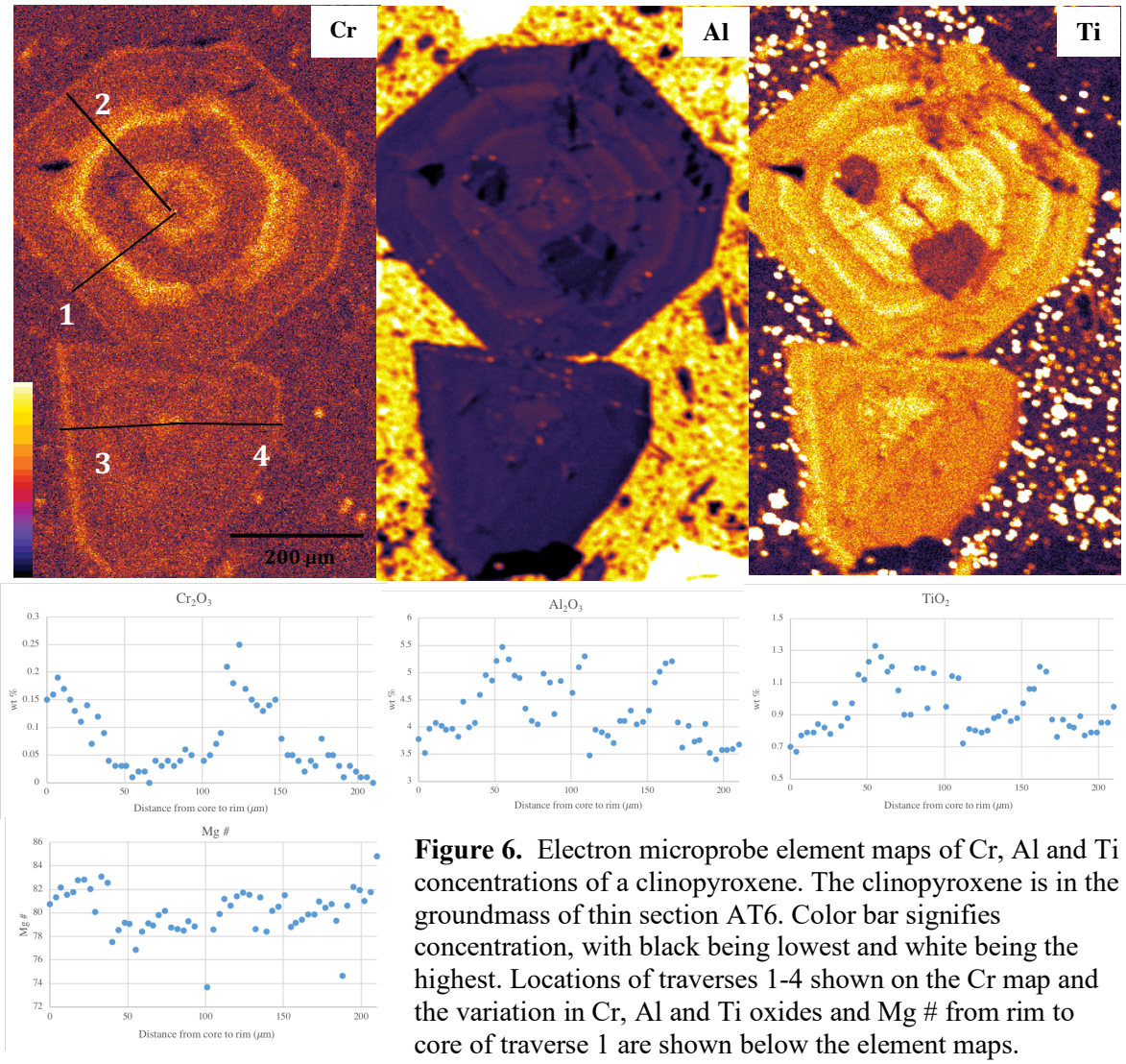

Figure 6. Electron microprobe element maps of Cr, Al and Ti concentrations of a clinopyroxene. The clinopyroxene is in the groundmass of thin section AT6. Color bar signifies concentration, with black being lowest and white being the highest. Locations of traverses 1-4 shown on the Cr map and the variation in Cr, Al and Ti oxides and Mg # from rim to core of traverse 1 are shown below the element maps.

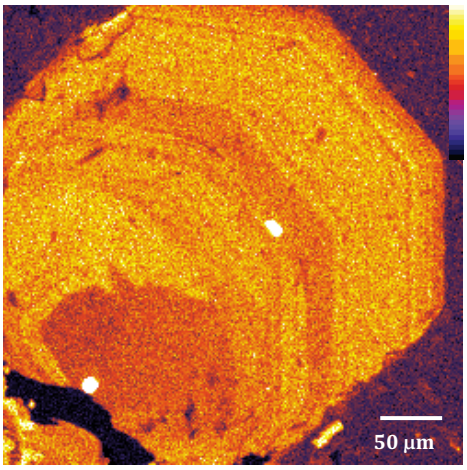

Figure 7. Electron microprobe map of Cr concentration in an orthopyroxene from a crystal cluster. The crystal is euhedral and has several distinct growth zones including a lower Cr core, middle zone and rim.

perhaps some subsequent modification by diffusion. Changes in Mg# positively correlate with the Cr concentration and vary from 74 to 85.

A ~350 μm pyroxene crystal from a cluster in the same thin section shows finer banding of Cr (Fig. 7). The entire crystal is more Cr rich than the crystals in the groundmass. There is a thick growth zone in the middle of the crystal that is less Cr rich as well as the rim and part of the core. No zoning was observed in Al or Ti. Traverses were made across crystals in the cluster for comparison with the clinopyroxene in the groundmass and thermobarometry, however all of the crystals are orthopyroxene. The steps between the spot analyses were too large to capture the changes recorded in the finer zoning, therefore compositional variation graphs were not generated. Clinopyroxene may have been too small in this cluster to observe with the microprobe or not present.

4.2 Trace Element Analysis of Hornblende and Clinopyroxene

Trace elements were collected from 32 plagioclase, 44 clinopyroxene and 32 hornblende crystals. Many of the trace elements were not abundant enough in the plagioclase to be used as a diagnostic tool, so only hornblende and clinopyroxene results are reported.

The hornblende and clinopyroxene crystals show similar trace element and rare earth element (REE) patterns, including positive anomalies for Ba, Pr, Nd, Sm and Zn, and negative anomalies for Cs, U, Pb, Sr, Zr, Ti, Li and Co. The trace elements in the hornblendes are 1-100 times more abundance than primitive mantle and about 1-200 times more abundant in the clinopyroxene. The REE patterns of both minerals show negative Eu anomalies and relatively flat heavy REE.

The hornblende crystals are all from the groundmass, but show some variations. The

REE pattern fans out towards the heavy REEs and several crystals show slight positive or negative anomalies in certain elements, such as Ho and Er, compared to the majority of the crystals. The trace element pattern of one crystal has higher abundances of heavy REEs, Pb, Cs and Rb but lower Ba, Sr, Zr, and Hf anomalies than the rest of the crystals.

The clinopyroxene from the crystal clusters are distinguishable from crystals in the groundmass by higher concentrations of most trace elements. A few clinopyroxene crystals show deviations from the majority including one groundmass crystal that has much lower trace element concentrations than all the others and a positive Li anomaly.

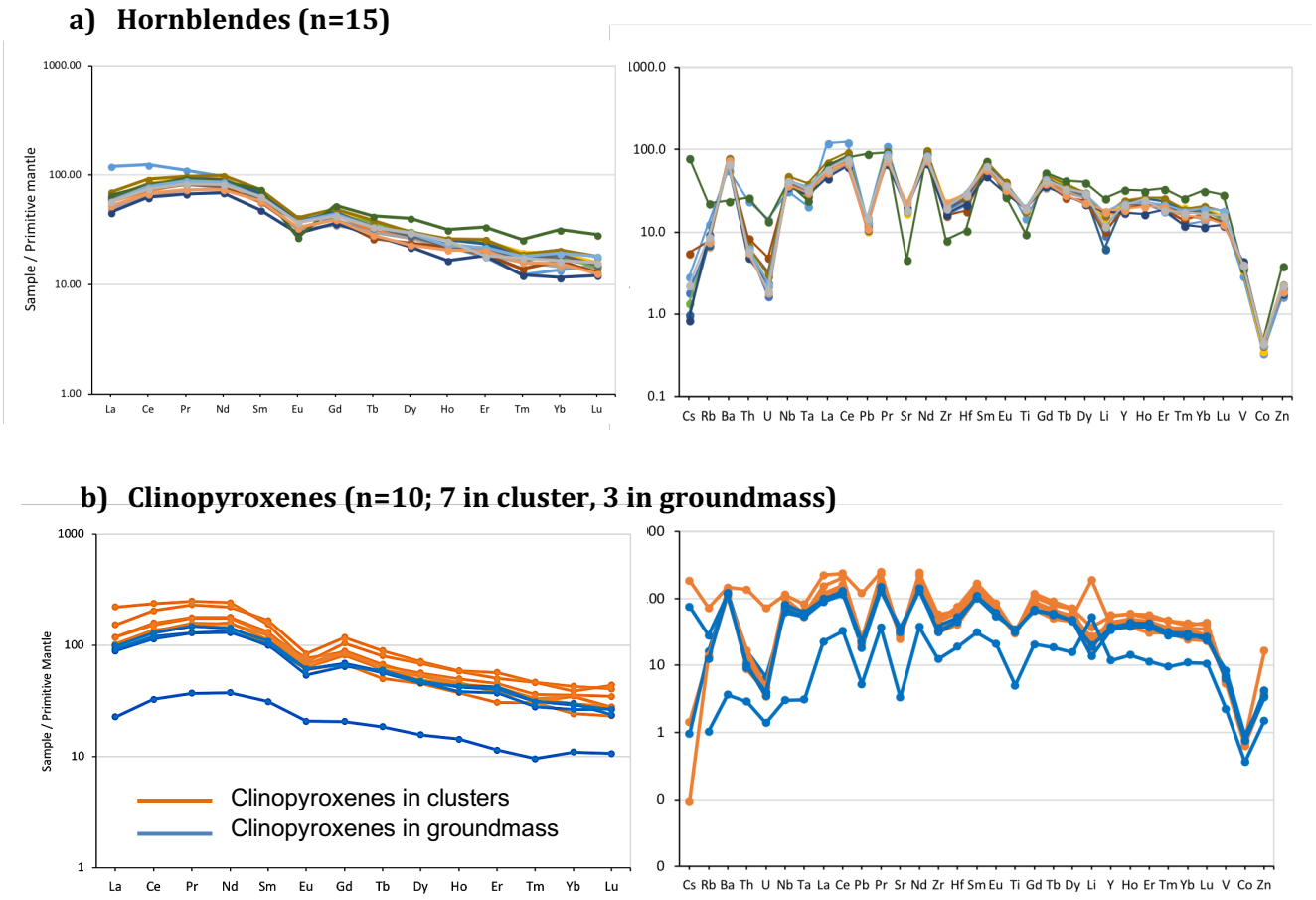

Figure 8. Primitive mantle-normalized Rare Earth Element and Trace Element patterns for hornblendes and clinopyroxenes. All 15 hornblendes were from the groundmass and show a similar REE pattern but some differences in the heavier elements and the incompatible trace elements. Clinopyroxenes in the crystal clusters and groundmass have similar patterns but differences in the concentrations.

One clinopyroxene grain in a crystal cluster has higher Cs, U, Th, Pb, La and Zn, and another has a positive Li anomaly. Generally, the hornblende clinopyroxene appear to have similar trace element and rare earth element patterns suggesting a common origin.

4.3 Rare earth and trace element concentrations of parent magmas from hornblende and clinopyroxene

Hornblende and clinopyroxene trace element compositions obtained through LA-ICP-MS and published partition coefficients (Appendix E) were used to determine the trace element composition of their parental melt. The parental melt calculated for hornblende has similar trace element abundances as the whole rock, particularly for the heavier trace elements (Fig. 9). The parental melt calculated for clinopyroxene had higher trace element abundances than the hornblende melt and whole rock but one calculated

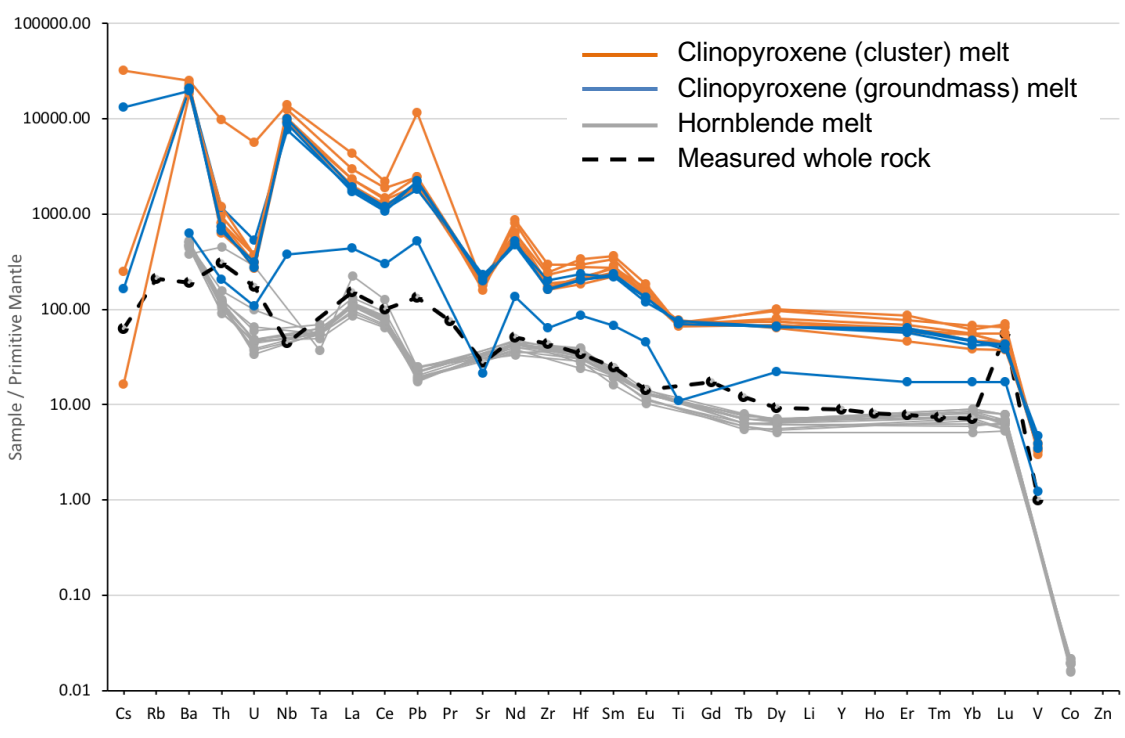

Figure 9. Trace elements of parental melts for hornblende and clinopyroxene. The concentrations were calculated from published partition coefficients and plotted with trace element data of the whole rock measured by Seaman (2000).

clinopyroxene melt had much lower trace element abundances near the whole rock and hornblende melt (Fig. 9). These results show that clinopyroxenes and hornblendes did not crystallize from the same parental magma, but hornblende may have crystallized from a magma similar to the whole rock composition.

4.4 Thermobarometry

4.4.1 Clinopyroxene Thermobarometry

The pressures and temperatures calculated from clinopyroxene crystals in the clusters and the groundmass generally overlap (Table 1). Seaman (2000) noted that the clinopyroxene in the groundmass covered a significant compositional range and this

Table 1. Clinopyroxene and clinopyroxene-melt thermobarometry calculations after Putirka (2008). Two representative crystals from the groundmass and two crystals from two clusters.

Clinopyroxene Host	Matrix 1	Matrix 2	Cluster 1	Cluster 1	Cluster 2	Cluster 2
Equilibrium Liquid	Trachy-basalt	Trachy-basalt	Basalt	Trachy-basalt	Trachy-basalt	Trachy-basalt
Test for Equilibrium						
Fe-Mg exchange	0.29	0.41	0.29	0.21	0.32	0.36
KD(Fe-Mg)	0.267	0.273	0.279	0.271	0.27	0.275
Barometers P(kbar)						
Eqn 30 ± 3.6	3.2	6.5	4.1	3.2	5.3	5.6
Eqn 31 ± 2.9	4.4	8	6.8	5.8	7.2	8.2
Eqn 32a ± 3.1	3	6.7	5.7	4.7	3.1	3.6
Eqn 32b ± 2.6	1.4	3.6	4.3	3.2	3.6	4.2
Eqn 32c ± 5	6.8	11.5	6.8	5.5	4.4	5.1
Thermometers T(C)						
Eqn 32d ± 58	1170	1159	1212	1204	1187	1191
Eqn 33 ± 45	1120	1147	1155	1126	1108	1128
Eqn 34 Sat. ± 45	1153	1187	1201	1169	1179	1198

Equations 32a, 32b, 32c, 32d based on clinopyroxene compositions only

If Fe3+ is significant, then the coefficient for Fe-Mg exchange should be something less than 1

Equilibrium liquid compositions from Kinzler, R.J., Grove, T.L. (1992)

Clinopyroxene analyses from Seaman (2000)

appears to be reflected in the large range of calculated pressures but not the calculated temperatures, which have a small range, or equilibrium melt compositions. Pressures for matrix 2 clinopyroxene is roughly double matrix 1 clinopyroxene. Crystals from the same cluster show variation in pressure and temperature. The first crystal from cluster 1 produces higher pressures (~1 kbar higher) consistently for all barometers and slightly higher temperatures than the second crystal and was in equilibrium with a basalt while the second was in equilibrium with a slightly more alkaline and silicic melt.

4.4.1.1 Groundmass Clinopyroxene: Single Crystal Traverse

Calculated temperatures, based on clinopyroxene composition only, were fairly uniform from the core to the rim of the clinopyroxene crystal (Fig. 11 and Table A.2, Appendix A). Pressure was more variable and has several peaks in the pressure at approximately 59, 101 and 166 microns from the core of the crystal. Based on the thermometer (Equation 32d) and barometer (Equation 32a) of Purtika (2008), the clinopyroxene crystallized at ~1200 ºC (± 58 ºC) and 4.1 – 7.6 kbar (± 3.1 kbar).

Temperatures and pressures calculated from mineral-melt equilibrium equations were similar to the values based on clinopyroxene only (Fig. 11). Pressures from both calculations followed a similar trend along the traverse, however, the temperature trends differed. The mineral-melt equilibrium produced three increases not seen in the clinopyroxene-based calculations.

Two estimates for the melt in equilibrium with the clinopyroxene were used to calculate the temperatures and pressures along the traverse of the crystal because the groundmass, magma envelope and enclave compositions did not pass the equilibrium tests (Fig. A.1, Appendix A). The equilibrium tests shows that one melt was not always

in equilibrium with the crystal throughout its entire growth history (Fig. 10). The crystal started growing from a higher Si, Al and lower Fe, Mg melt and had two subsequent periods when it was in equilibrium with a lower Si, Al and higher Fe, Mg melt.

Table 2. Estimates for groundmass clinopyroxene equilibrium melts for thermobarometric calculations. Groundmass, envelopes and enclave compositions from Seaman (2000). Estimates determined using equilibrium tests of Piturka (2008).

wt%	Groundmass	Magma Envelopes	Enclaves	Estimate 1	Estimate 2	Estimate 3
SiO_2	67.76	64.70	63.50	51.00	47.80	53.00
TiO_2	0.41	0.14	0.50	2.40	1.50	2.80
Al_2O_3	18.26	17.02	17.40	10.00	19.10	11.00
FeO	0.66	0.55	6.30	11.50	11.50	9.00
MnO	0.04	0.03	0.20	0.40	0.12	0.45
MgO	0.92	0.20	2.10	6.50	6.10	6.00
CaO	2.46	3.06	3.10	10.00	9.30	10.00
Na_2O	4.06	6.41	3.80	6.50	4.10	6.50
K_2O	4.10	3.46	3.10	1.00	0.35	1.00
Cr_2O_3	0.00	0.00	0.00	0.10	0.09	0.08
H_2O	2.28	2.29	2.38	0-2	0-2	0-2

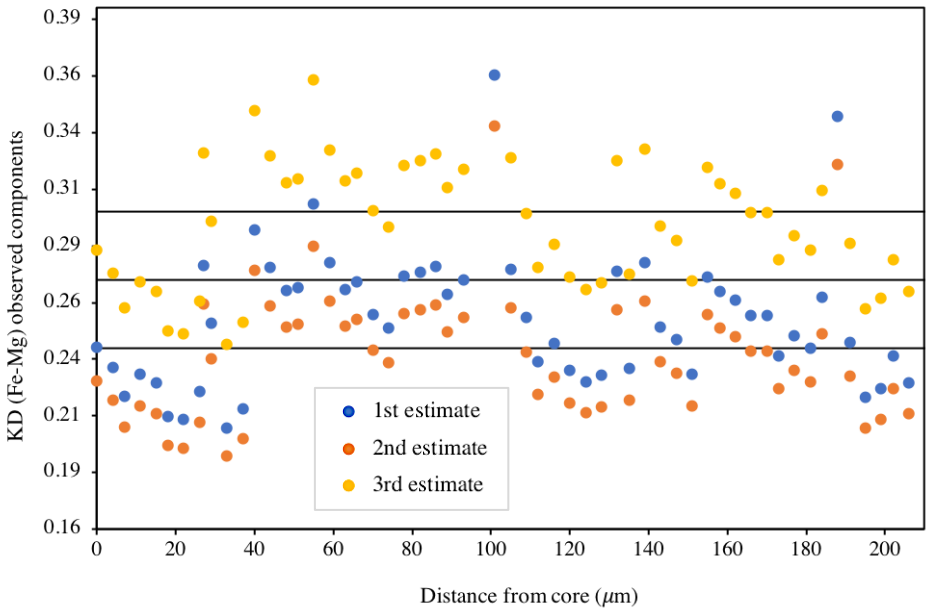

Figure 10. KD values for the three estimated equilibrium melts. KD values vary with composition of the crystal along the traverse. This demonstrates that more than one melt was in equilibrium during the crystal's growth.

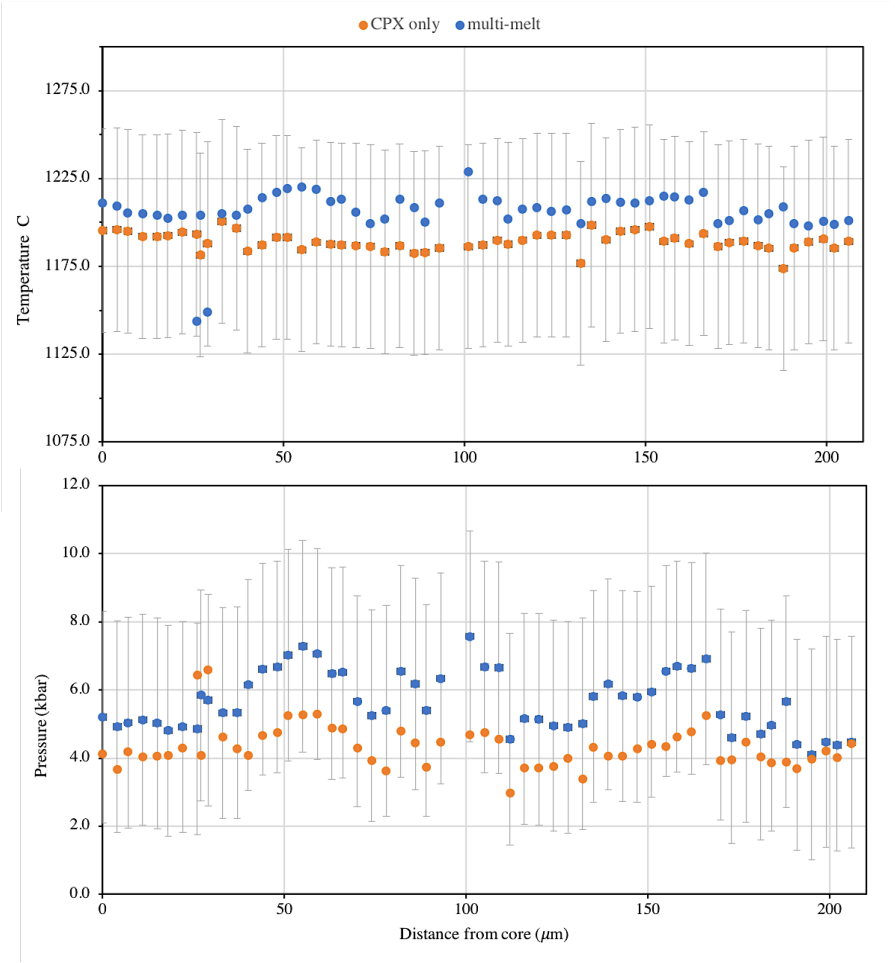

Figure 11. Temperature and pressure across a zoned clinopyroxene in the groundmass. Calculations of temperature and pressure made using the single crystal thermobarometer (orange) with the corresponding error bars and using the clinopyroxene-melt thermobarometer where the equilibrium melt has to vary along the traverse.

4.4.2 Orthopyroxene Thermobarometry

The large step size in between analyses along the traverses of the orthopyroxene in the cluster may not have captured all the detailed of the finer zoning, therefore graphs of pressure and temperature variations are not made for the traverses of the crystals.

Thermobarometric calculations were performed for three traverses that had high Cr concentrations (Appendix B). Pressures obtained with the barometer based only on the orthopyroxene components (Equation 29c) range from 1.1 to 2.5 GPa (~40.7 – 92.5 km).

The saturation temperature for the anhydrous equilibrium melt was 1378-1450 °C and crystallization temperatures for the orthopyroxene based on the anhydrous melt were 1321-1496 °C. When 3 wt. % H_2O is added to the melt, the temperatures and pressures decrease. Pressures decrease to 0.7-1.9 GPa (25.9-70.3 km), the saturation temperature decrease to 1305-1379 °C and crystallization temperatures decrease 1261-1419 °C.

4.4.3 Hornblende Thermometry

The average calculated temperature of hornblende crystallization from the groundmass is 970 °C at a pressure of 342 MPa. Hornblende in/near a crystal cluster, magma envelope or enclave record a slightly lower average temperature and pressure (Table 3.). There is one "outlier" in the groundmass that has the highest temperature and pressure of all the hornblende crystals analyzed, owing to its high Al_2O_3 wt% (Fig. 12). Excluding this point changes the average temperature to 968 °C with the same pressure, therefore has negligible effects, and is well within the error of the calculations. The "outlier" of the hornblende in magma envelopes has the lowest Al_2O_3 wt% and excluding this point again, produces new averages within the error of the original. The calculated average H_2O wt% of the parental melt from which hornblende crystallized was similar for all hornblende in the different components.

Table 3. Hornblende average physical-chemical parameters. Ridolfi et al. (2010) thermobarometric equations were used to calculate crystallization conditions for hornblendes in the groundmass, clusters and magma envelopes.

Lava flow component hosting hornblende	T (°C) ± 22	P (MPa)	Depth (km)	ΔNNO	logfO2 ± 0.4	H_2O_{melt} (wt.%)
Groundmass	970	342 ± 38	12.7 ± 1.4	0.7	-10.0	3.8
Cluster	962	329 ± 36	12.2 ± 1.3	0.8	-10.0	3.8
Envelope	955	305 ± 34	11.2 ± 1.3	0.8	-10.2	3.9
Between enclave & cluster	969	336 ± 37	12.4 ± 1.4	0.8	-9.9	3.7
All data (n=34)	967	335 ± 37	12.4 ± 1.4	0.7	-10.0	3.8

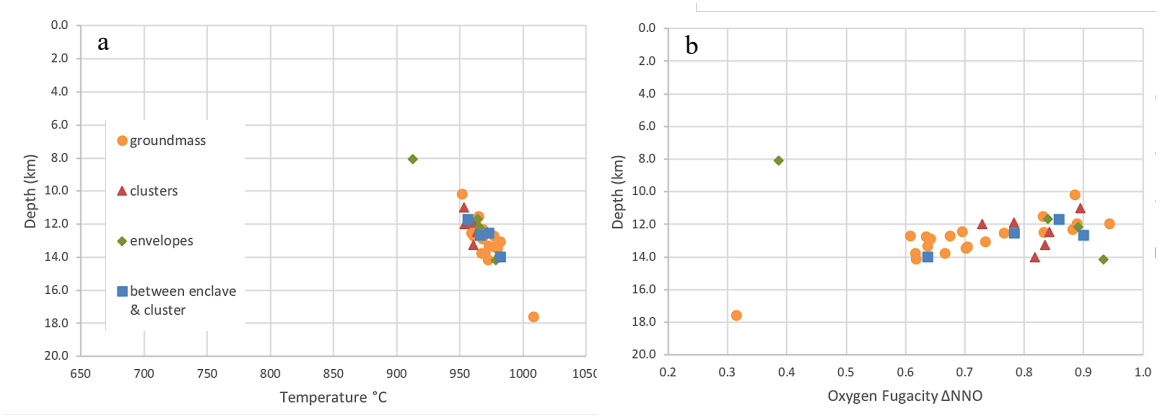

Figure 12. Variations of hornblende crystallization. Plots of a) temperature vs depth and b) oxygen fugacity vs depth for all hornblende calculations. Temperatures are well constrained between 950-980°C. Oxygen fugacity displays a range between 0.6 and 0.95.

4.4.4 Plagioclase-melt Thermobarometry

The plagioclase in enclaves record the lowest calculated temperatures (970-1029 ºC) with an equilibrium melt having an enclave composition and 2.5-3 wt.% H_2O (Fig. 13 and Table C.1, Appendix C). The dusty, honeycomb and cluster plagioclase had the highest temperatures (1057 – 1096 ºC) The honeycomb and cluster plagioclase had a corresponding anhydrous trachyandesite equilibrium melt while the dusty plagioclase had either a more silicic or mafic equilibrium melt. Clear, euhedral phenocrysts of plagioclase in the groundmass have a temperature range of 100ºC (992-1078 ºC) using two different melt compositions and variable water content and many of these overlap within error (± 36ºC). Also all calculated pressures based on groundmass plagioclase are less than 3 kbar. Groundmass lath temperatures also overlapped with the phenocryst temperatures with exact melt compositions and water content but at slightly lower pressures and temperatures. This supports the hypothesis of Seaman (2000) that laths grew later than the phenocrysts during ascent to the surface. Also the relatively small difference in temperatures between the groundmass and enclaves shows that the enclaves contain

larger crystals because they were able to cool slowly rather than rapidly chill. Each calculation for the honeycomb rims was done using a different equilibrium melt composition. The temperatures are fairly uniform and within error (1039-1054 ºC) but the pressure differs significantly (12.2-2.2 kbar). Increasing the estimated water content of the equilibrium melt resulted in in the calculated pressures decreasing for each plagioclase (Fig. 13). These results suggest that plagioclase crystallized over a range of depths and temperatures from different parental melts.

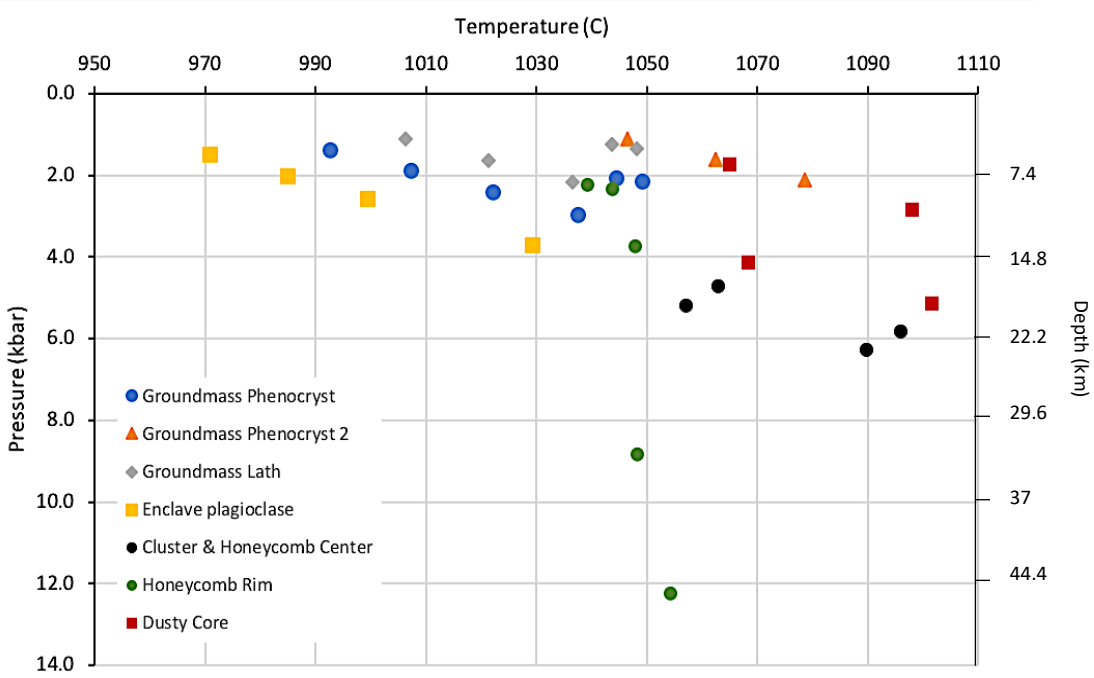

Figure 13. Results of plagioclase-melt thermobarometry. The different textural and compositional types of plagioclase show a clear pressure-temperature relationship.

4.4.5 Zircon Saturation Thermometry

To assess the zircon saturation temperatures we first need to consider which model is most appropriate and evaluate whether the melt composition fits within the compositional range the model was calibrated for. The compositional parameter, M, for

the whole rock analyses, ranges from 1.87 to 2.10 (Table 4.) which is at the high end or exceeds the calibrated compositional range of the Watson and Harrison (1983) and Boehnke et al. (2013) thermometers. The M value for the groundmass is 1.71 and lies within the compositional range of these thermometers. All G values for the whole rock and groundmass were in the calibration range for the Gervasoni et al. (2016) model. The four thermometers produce a narrower temperature range (45°C) for the groundmass than the whole rock (150°C) which would be in the estimated error of ± 50°C (Table 4.). For each thermometer the temperatures are highest for the groundmass composition and, for a given composition, highest using the Watson and Harrison (1983) thermometer. Based on the composition parameters and calibration range of the models, the saturation temperature calculated for the groundmass using the Gervasoni et al. (2016) thermometer is likely the most representative.

Table 4. Temperature calculations for zircon saturation. The whole rock and groundmass compositions measured by Seaman (2000) were used in four thermometers. The appropriate model is chosen based on the compositional parameter M or G.

Thermometers	Calculated Temperature (± 50°C)			
	Whole rock			Groundmass
*Watson and Harrison (1983)	846	834	833	861
Hanchar and Watson (2003)	840	828	827	855
*Boehnke et al. (2013)	793	774	771	816
*Gervasoni et al. (2016)	723	709	696	832
Compositional Parameters				
M (Na+K+2*Ca)/(Al*Si)	1.87	2.02	2.10	1.71
G $(3\cdot Al_2O_3+SiO_2)/(Na_2O+K_2O+CaO+MgO+FeO)$	5.16	4.85	4.41	7.97

Watson and Harrison (1983) and Boehnke et al. (2013) was calibrated for compositions between $1 \leq M \leq 1.9$ and work well in mostly aluminous melt compositions between $1.3 \leq M \leq 2$
Gervasoni et al. (2016) was calibrated for compositions $3 \leq G \leq 16$
* T < 800 °C is outside the calibrated range for these 3 models, and will result in higher uncertainties due to extrapolation. The exact nature of the uncertainties is unclear, but estimated temperature uncertainties are on the order of at least 50 °C. (Gervasoni et al., 2016)

Zr concentration of the groundmass has not been directly measured so the above calculations were performed with the average Zr concentration of whole rock measurements (467 ppm) from Seaman (2000). Zircon saturation temperatures were then calculated with Gervasoni et al. (2016) varying the Zr concentration. This produced an upper limit of ~904 °C at 700 ppm and lower limit of ~753 °C at 300 ppm for the groundmass composition (Appendix D).

4.4.6 Thermobarometry Summary

When all of the thermobarometric results are combined, distinct depths and temperatures at which each mineral crystallized (Table 5) are readily apparent and parental melt compositions evolve following those trends (Fig. 14). Orthopyroxene in clusters crystallized at depths greater than 25 km, in the upper mantle, at the highest temperatures, from the most mafic parent estimated to be a picro-basaltic composition. Clinopyroxene then crystallized at 11.5 – 30 km, lower temperatures and from a more evolved parent of basalt or trachybasalt composition. Plagioclase crystallized throughout the crust from 4-23 km at a range of temperatures and parent melts. Zircon saturation occurs between the crystallization of the groundmass and hornblende. These results show that the components of the Atascosa Lookout lava flow crystallized at various levels of the crust and not all in a single magma chamber at one depth as well as from significantly different parental melts.

Table 5. All mineral thermobarometry results.

Component	Host	Temperature °C	Pressure (kbar)	Depth (km)
Groundmass*	---	801	--	--
Zircon Saturation	Groundmass	753 - 904	--	--
Hornblendes	Groundmass	948 – 992	3.04-3.80	11.3 - 14.1
Hornblendes	Cluster	940 – 984	2.93-3.65	10.9 - 13.5
Hornblendes	Envelope	933 – 977	2.71-3.39	9.9 - 12.5
Hornblendes	Between enclave & cluster	947 – 991	2.99-3.73	11 - 13.8
Plagioclase	Enclaves	970 - 1029	1.4-3.6	5.3 – 13.5
Clear Plagioclase	Groundmass	992 - 1078	1.1 – 5.7	3.9 – 21.2
Plagioclase Laths	Groundmass	1006 - 1048	1.1 – 2.1	3.9 – 7.8
Honeycomb Plagioclase Rim	Glomerocyrst, Groundmass	1039 - 1054	2.2-12.2	8.1 - 45
Center of Honeycomb & Plagioclase Cluster	Glomerocryst, Groundmass	1057 - 1096	4.7 – 6.2	17.3 – 23.1
Dusty Core of Plagioclase	Groundmass	1065 - 1101	1.7 – 5.1	6.3 – 18.9
Clinopyroxene	Groundmass	1075 - 1232	1.4 – 6.5	5.0 - 25.0
Clinopyroxene	Cluster	1063 - 1270	3.1 – 8.2	11.5 - 30
Orthopyroxene	Clusters	1261-1419	11 – 25	25.9-70.3

* Calculation of groundmass crystallization from Seaman (2000)

Depth calculations using 2.3 g/cm^3 as density for rock

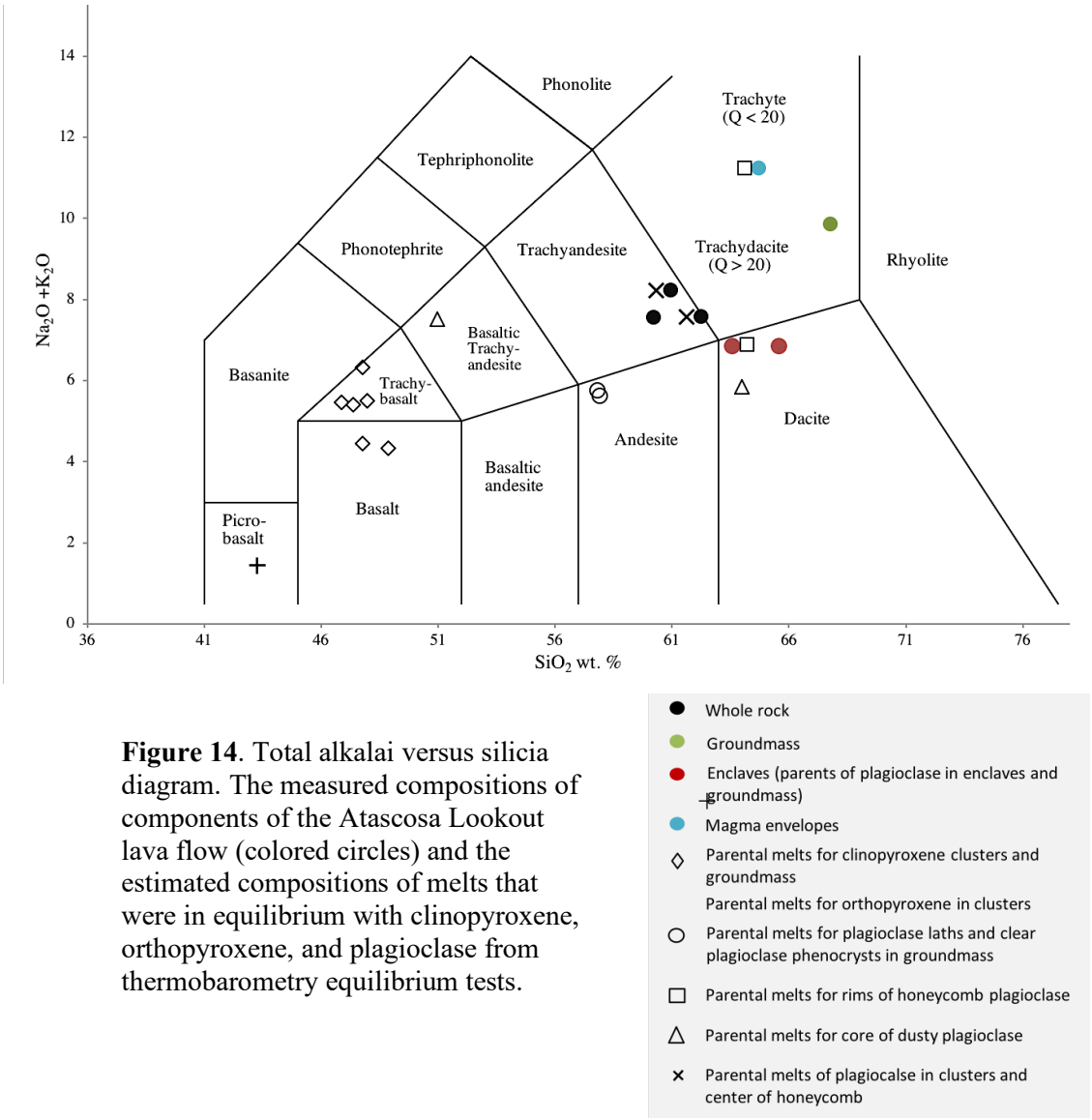

Figure 14. Total alkalai versus silicia diagram. The measured compositions of components of the Atascosa Lookout lava flow (colored circles) and the estimated compositions of melts that were in equilibrium with clinopyroxene, orthopyroxene, and plagioclase from thermobarometry equilibrium tests.

4.5 Zircon U-Pb Ages

U-Pb ages and cathodoluminescence (CL) images were obtained from zircon in thin section ATCX3b from the groundmass and inside a hornblende crystal (Table 4). The CL images of zircons 1,2 and 5 (Fig. 15) show zoning and zircon 2 has a truncated surface. The zoning could indicate periods of growth and in fact dates taken from different areas of the grains have different ages including error. The total range of all zircon dates in the

matrix (1, 2 and 5) is 22.4 my to 25.7 my. Zircon 1 gives U-Pb ages between 22.4 Ma (bottom rim, Fig. 15) and 24.9 Ma (top rim, Fig. 15) but given the earliest eruption age of the lava flow is 23.3 Ma based on $^{40}Ar/^{39}Ar$ of sanidine, the date of the south rim may not be valid or the $^{40}Ar/^{39}Ar$ may be slightly in error. The left end of zircon 5 could be as old as 25.7 or 24.7 my. and the right end could be as young as 23.2 or 24.2 my, with the actual cutoff being 23.3, the time of eruption. The shortest span of zircon growth recorded by this zircon could potentially be 0.91 my (24.7 – 23.79).

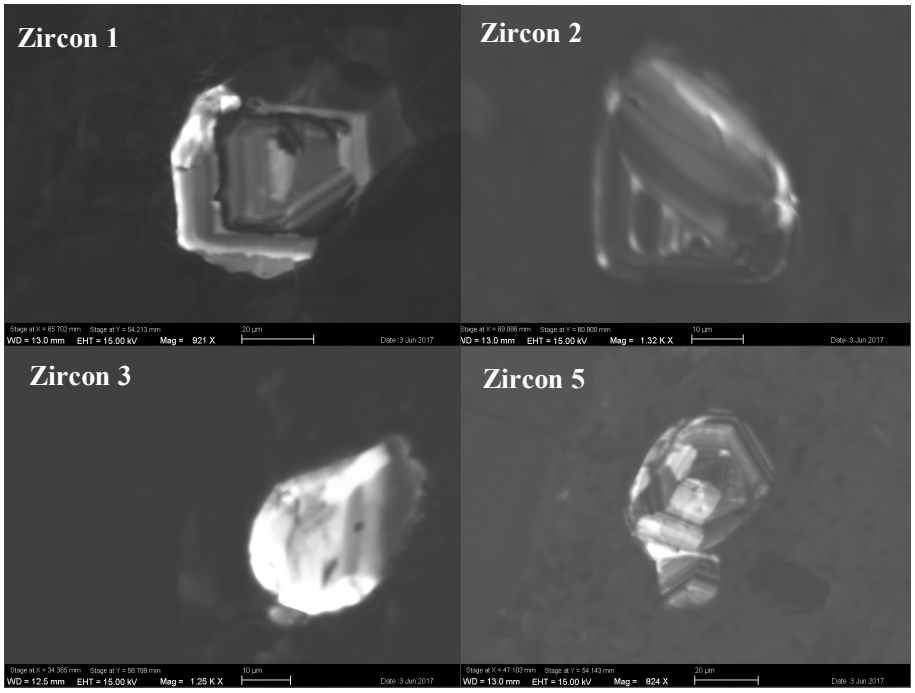

Figure 15. Cathodoluminescence images of zircons analyzed for U-Pb ages

Table 6. Zircon U-Pb ages. Four zircons in the groundmass and a hornblende crystal were analyzed. For comparison, argon age dating of hornblendes produces an age of ~23.8 Ma.

Analysis	Spot	Age (Ma)	Host	Spot Location
zircon 1	32	22.8 ± 0.4	Groundmass	Bottom rim
zircon 1	33	23.4 ± 1.5	Groundmass	Top rim
zircon 2	29	23.8 ± 1.4	Groundmass	
zircon 3	35	24.2 ± 0.8	Hornblende	Inside hornblende
zircon 5	14	23.7 ± 0.5	Groundmass	Right rim of zircon
zircon 5	13	25.2 ± 0.5	Groundmass	Left rim of zircon

CHAPTER 5

DISCUSSION

5.1 Implications of textures and mineral compositions

The texture of a rock records various processes that controlled the rock's evolution and provides the information to interpret the rock's origin and history together with mineralogy and chemical composition (Winter 2001). The disequilibrium textures observed in this study with the SEM add to the variety of textural variations documented by Seaman (2000) which established that some components of the flow probably did not crystallize from the groundmass. The enclaves are the most direct evidence of open system behavior, because they are the result of incomplete mixing. Embayments in crystals can also be caused by magma mixing or the drop in pressure during magma ascent (Winter, 2001). The gradual loss of pressure that releases volatiles from hydrous magma may be the cause of oxides that are prevalent in the wispy patches of trachydacite that occur throughout the groundmass and surrounds some enclaves, plagioclase glomerocrysts and crystal clusters (Winter, 2001). Differences in size, position of inclusions, and composition zoning indicate that the dusty and honeycomb plagioclase crystals had different histories. Additionally, there are two assortments of crystal clusters, one composed of clinopyroxene, orthopyroxene and plagioclase and another of quartz, pyroxene, calcic plagioclase and hornblende that probably did not crystallize from the same magma.

Hornblende rims were previously noted but this study documents the range of rim thickness and breakdown of hornblende that occurs. A recent study by De Angelis et al. (2015) showed that thickness of reaction rims by themselves cannot distinguish between

decompression and heating. However, the rim mineralogy can be used to potentially discriminate between those processes. Decompression or long heating events should result in rims containing Fe-rich orthopyroxene while short heating events would produce rims favoring Ca-rich clinopyroxene (De Angelis et al., 2015). The rims were geochemically analyzed by Seaman (2000) and found to have higher Fe and lower Ca which may rule out a short heating event.

A surprisingly radiating texture of several chromium clinopyroxenes occurs in two thin sections that were prepared for this study. The texture is reminiscent of spherulites, that are radiating arrays of crystal fibers resulting from the high-temperature devitrification of natural glass (Lofgren 1971). Devitrification involves the nucleation and growth of crystals at subsolidus temperatures and pyroxene and/or plagioclase fibers result from cooling mafic glass (McPhie et al., 1993). The general shape of the crystal mass is temperature dependent and crystal fiber width will increase with higher temperatures and isolated spherulites are commonly spherical (Lofgren 1971). Most importantly, the radial pyroxenes, like the enclaves, represent direct evidence of a distinct magma and incomplete mixing.

5.1.1 Zoning in Pyroxene

The zoning of chromium, aluminum and titanium in the clinopyroxene and chromium in orthopyroxene is a new observation. Zoning or growth bands in single crystals have been interpreted as reflecting crystallization from more mafic magmas after initial growth in a more silicic magma (i.e. recharge event) and preservation of zoning is controlled by volume diffusion in the crystal, which for Cr in the pyroxenes is relatively slow (Costa & Morgan, 2011; Orman & Grove, 2001; Streck, 2008). Coarse, thick growth zones are

interpreted as a reflection of dynamic magmatic processes while fine banding is interpreted to be kinetically controlled (Streck, 2008).

The different zoning patterns of the clinopyroxene in the matrix and the orthopyroxene in the clusters suggests that these crystals grew in different environments. The orthopyroxene may have grown from a magma that had lower Cr and then experienced two injections of new magma that created growths zone with higher Cr. Conversely, the clinopyroxene grew first from a magma with relatively high Cr and then continued growth in a lower Cr magma, punctuated by a high Cr growth zone and a high Cr rim. The thermobarometry confirms the different pressure and temperatures of their growth environments as well as the parental melts with which they were in equilibrium.

The thin (~10 μm), high-Cr rim of the groundmass clinopyroxene suggests short growth after an injection of hotter, more mafic magma into its reservoir. The formation of this rim may have taken less than 2 days, according to clinopyroxene growth rates on the order of 10^{-8} cm/s calculated for Mt. Etna trachybasalts (Orlando et al, 2008). Growth rates can be even faster under degassing and high undercooling at shallow depths but would produce dendritic and other anhedral crystals (Mollo et al., 2010) that are not observed, so this growth rate is taken as a maximum. The implications of this growth rate is that the magma that generated this clinopyroxene may have come from as deep as the crust-mantle transition zone, around 25 km, to the surface in a very short period of time.

5.2 Trace and Rare Earth Element Analyses in Hornblende and Clinopyroxene

The major element composition of the crystal dominates the incorporation of the trace elements while P, T and fO_2 influence trace element partitioning to a lesser extent (Marks et al., 2004). The uniform variations in the rare earth element concentrations and patterns

of the hornblende and clinopyroxene crystals would suggest they each crystallized from similar melts that were evolving as crystallization took place and the melt changed composition. The hornblendes are visibly different in size and texture, with some having thicker reaction rims, indicating that the hornblendes possibly grew continuously over a relatively long time period. The narrow crystallization depth of 12-13 km and the compositional similarity of hornblende crystals in the groundmass and clusters suggest all these crystals grew from the same magma. The range in temperature and oxygen fugacity calculated for hornblendes in the groundmass suggests crystallization conditions for these hornblendes were partly heterogeneous.

The trace elements have less uniform patterns with significant differences in the pattern and abundance of some crystals. This could mean either the magma body was heterogeneous or some crystals evolved in separate magma bodies in the crust that had similar but slightly different compositions and/or histories.

The clinopyroxene crystal from the groundmass that has a significantly lower concentration of trace elements was not observed to be in an especially different setting than the others. The discovery of zoning of clinopyroxenes in this study could mean that there are significant trace element variations within individual clinopyroxenes which might be the cause of trace element variations observed. The measurement could also be an erroneous measurements and due to instrument error or drift, as it was the very last analysis of the session.

5.3 Parent magma compositions

The compositional zoning of the groundmass clinopyroxene resulted in a range of possible magmas that were in equilibrium with the crystal during its growth. The range of

magmas is restricted in $\%SiO_2$ but varies more in alkali content (Fig. 14). By analyzing the traverse of a single crystal we can access more of the history of the parental magmas. The thermobarometric calculations, did not differ significantly between those based solely on the clinopyroxene composition and those based on the equilibrium melt and clinopyroxene composition. This is important to note because of the time and effort that goes into estimating the equilibrium liquids when they are entirely unknown; one can simply obtain the pressures and temperatures by using the clinopyroxene analyses themselves. The magmas found to be in equilibrium with the other clinopyroxene analyses, that consisted of just a single spot analysis, also fall into the same range but would be able to provide a richer history of their growth with thermobarometry on traverses and perhaps provide a better picture of the magma plumbing system.

All of the orthopyroxene crystals showed significant changes only in Cr and, as a result, a single estimated magma composition appears to be in equilibrium along the entire traverse of each crystal. However, the distance between each microprobe analyses along the traverses were also larger than those of the clinopyroxene traverse and could be averaging out differences, or skipping zones that differ enough in composition that would require different equilibrium melts.

The plagioclase, with its variety of textures, also has a variety of parental melt compositions. There are five estimates of parental melt compositions that differ significantly from one another and sometimes for the same component, such as the core of the dusty plagioclase which can be in equilibrium with either a dacite or a basaltic trachyandesite based on the equilibrium tests. However, Seaman (2000) noted the dusty plagioclase have a high calcium core suggesting it originated in a relatively more calcic

magma. The basaltic trachyandesite has ~10% CaO compared to the ~4% of the dacite which means it may be closer to the true equilibrium melt for the core of the dusty plagioclase. After the basaltic trachyandesite, the estimates for the other components spread out in alkali and silica content suggesting that the rest of the components evolved in separate pockets of magma. In particular, the enclaves represent a distinct magma that is closer in composition to the whole rock than the groundmass or any of the other estimated melts.

5.4 Variations in crystallization temperature and pressure

Our ability to calculate exact temperatures and pressures for igneous rocks, as compared to metamorphic rocks, is more difficult due to the larger amount of liquid present relative to crystals. The liquid may have less compositional stoichiometric constraints and may pass through changes in pressure, temperature without precipitating a new phase due to their ability to expand, contract and mix (Putirka, 2008). However, many thermobarometry calculations have been recently supported by independent observations such as seismic studies at active volcanoes (e.g. Geiger et al., 2016; Ubide & Kamber, 2018).

The thermobarometry calculations in this study were mostly performed from spot analyses on single crystals and averages of numerous analyses. However, we know from the electron microprobe element maps made in this study that the pyroxene are zoned, particularly with respect to Cr. Therefore, it is reasonable to ask whether we have an accurate picture of the crystallization depths and the magma plumbing system. The traverse of the single clinopyroxene show variations of 30-60 ºC, which is close to the error of the equations, and variations of 3-7.6 kbar which exceeds the error of the

equations. The orthopyroxene traverses have variations in pressure up to 10 kbar and 158ºC which both exceed the error for the equations used. The pressure differences are generally correlated to the temperature, where they both increase or decrease simultaneously suggesting these crystals are forming as they ascend and/or some other process such as magma injection changes the conditions of the magma reservoir or overturns the magma.

5.5 Zircon age and thermometry

The zircon saturation temperature range of the groundmass lies mostly between the crystallization temperature of the groundmass and hornblendes. Zircon crystallization just before the groundmass and close to eruption is supported by some of the U-Pb ages and small size of the zircon. However, the observation that zircon are included in hornblende crystals contradicts this. The U-Pb age of a zircon inside a hornblende (Zircon 3, 24.2 ± 0.8 Ma) compared to the Ar ages of hornblende suggests that there is an older population of zircon that is either from a previous phase of magmatism or, alternatively, zircons crystallized more or less continuously from the earliest emplacements of magma that became incorporated into the Atascosa Lookout lava flow ~900 ky.

There are a few general principles that we can use to interpret the presence, age and temperature data of the zircon in the Atascosa Lookout lava flow. First, zircons that are present and preserved outside of any other mineral phase (i.e. in the groundmass or in contact with melt) indicate either short-residence times or an initially large size because they would have been resorbed or dissolved by the higher temperatures (Watson, 1996; Siégal et al 2018). Therefore, zircon in the groundmass of the Atascosa either crystallized

from the groundmass and near the time of eruption or crystallized much earlier in another part of the magma system and were originally bigger but decreased in size by interacting with new Zr undersaturated melt. The euhedral appearance of zircon in the backscatter electron images would suggest they crystallized from the groundmass.

Second, zircon growth commonly occurs in silicic or at least intermediate magmas and therefore igneous rocks with <64% SiO2 should lack autocrystic zircons (zircons that crystallized from their host liquids) (Siégal et al 2018). The groundmass of the lava flow is ~67% SiO_2 and could be close to the magma composition that zircons crystallized from. Underlying units in the Atascosa Formation are mainly rhyolitic in composition and any magma that remained in the crust during the those previous eruptions may also be the parental magma for the zircons (which would have different zircon saturation temperatures). The high geothermal gradient that is expected to have existed >23 Ma would have slowed the rate of magma solidification, allowing zircon crystallization to take place closer to the time of eruption of the Atascosa Lookout lava flow.

Third, mismatches between textures and compositions in cathodoluminescence images and age have been documented as a result of complex responses of U, Th and rare earth elements near the surface of the zircons that do not have any age significance (Siégal et al 2018). Additionally, zircon zoning does not always equal simple closed system crystallization, but can be a result of open system processes (Siégal et al 2018). The zoning of the Atascosa zircons and the truncation and deposition of new growth surfaces of zircon 2 may, or may not, reflect periods of Zr under-saturation in the magma due to mixing or recharge because the zircons appear euhedral in backscatter images which would contradict interaction with hotter, mafic magma.

Finally, zircon saturation temperature is a theoretical temperature predicting when zircon crystallization occurs and is only relevant as a thermometer when the bulk composition of the rock is close to the parental melt of the zircons (Siégal et al 2018). With the current information, it is uncertain whether the groundmass is the parental melt or if it is a hybrid of rhyolitic parental melt and a mafic injection shortly before eruption. And at < 25 MPa, pressure has no effect on zircon saturation (Siégal et al 2018) so zircon could have crystallized throughout much of the crust from various stages of previous magmatism. Therefore, in order to get a better idea of zircon crystallization, microprobe analyses of zircons should be performed in order to use the Ti-in-Zr thermometer.

5.6 Tectonic Influence on the Atascosa Lookout Lava Flow

The equation of Putirka and Platt (2012) has extension beginning in southern Arizona around 31.9 Ma and Goodwin & Haxel (1990) put the beginning of volcanism in the Atascosa-Tumacacori-Cerro Colorado complex just before the detachment phase of metamorphic core complex development in the Baboquivari Mountains to the west. The formation of metamorphic core complexes is favored by continental crust thickened by earlier collisional processes which heat up the crust by radioactive decay, causing the crust to become weak and fail (Ring, 2014). Core complexes also start forming in low-viscosity lower crust when extension occurs at high rates (Ring, 2014). Extensional tectonics also generates faults, creating pathways for magma to rise to the surface (Cassidy et al., 2015). Together, the extension and core complexes suggest favorable conditions to the ascent of magma through the crust of southern Arizona.

The roll back and/or break-up of the Farallon plate contributed to the thinning of the crust because the Farallon plate had been subducting at a very shallow angle and had floated more or less against the base of the crust. Mantle returning in its place, rising to shallower depths, could then produce the source of the magmas that would generate the volcanics of the Montana Peak and Atascosa Formations. In fact, the mantle may have mixed with material having high $^{87}Sr/^{86}Sr$ ratios from the subducting slab, and partial melting of a crust-contaminated mantle could produce melts with a variety of isotopic compositions (Lustrino & Anderson, 2015) This may be an alternative explanation to the assimilation of crustal material for the contrasting initial Sr isotope ratios observed by Seaman (2000) for crystals from different components of the lava flow. Due to previous magmatism and potential pathways for the ascent of magma, it is possible that the magma ascended rapidly through the crust with little crustal assimilation. Therefore another explanation, based on the different parental melts estimated for the different components of the lava flow, is that the different $^{87}Sr/^{86}Sr$ ratios reflect the different crystallization environments these components originally crystallized in. Different magma pockets may have contained crystals or liquid that previously incorporated crustal material.

Many other mid-Cenozoic volcanic sequences in the western US share the progression from voluminous felsic breccias, pyroclastics and interbedded lava flows to basaltic andesites which have been termed the Southern Cordilleran Basaltic Andesite Suite (Cameron et al., 1989; Spencer et al., 1995) that is present in the Atascosa Formation. This appears to indicate a tectonic influence on the composition of the magma that produced the Atascosa Lookout lava flow. Additionally, models of the evolution of magmatic systems proposed by Annen et al. (2006) and others show that a system can

become less evolved with time as it is heated when more basalt, or more primitive magma, is injected into the system. Hotter rocks are able to act in a less viscous manner and accommodate the deformation associated with high emplacement rates of magma (Menard 2011). This suggests it is possible that the Atascosa Lookout lava flow was assembled and rose quickly to the surface, giving it less time to fractionate out more mafic components.

5.7 Magma Plumbing Model

A schematic representation of the magma plumbing model that produced the Atascosa Lookout lava flow is shown in Figure 16. In the proposed model, batches of magma/crystalline mush are present throughout the crust, including remnants of older magmatism. The locations of the batches are partly influenced by the major lithology changes within the crust that represent the major tectonic and volcanic stages. The exact depths of the selected geologic units of the model are unknown but are estimated based on length of time they represents and possible correlation to magma reservoir depths because lithology changes would be potential barriers to magma ascent. The normal faulting and drop down of the block that part of the Atascosa Lookout lava flow is on occurred after the flow was emplaced, though the faults may have started to develop around the time of the flow and may have influenced or been influenced by magmatism. The location of the vent or opening from which the lava flow erupted is unknown and may not be represented by any of the outcrops preserved.

The Atascosa Lookout lava flow began as mafic injections from the mantle (picro-basalts) that stalled at the base of the crust and evolved to trachybasalts. The

magma was then buoyant enough to rise through the crust-mantle transition, carrying crystal clusters containing orthopyroxene. The lower to mid-crust was dominated by clinopyroxene and plagioclase mushes from earlier ascending magma and the mid-crust was the likely storage zone and site of hornblende crystallization. Enclaves may have been small pockets magma stored along the path of the ascent above where hornblende was crystallizing. A high geothermal gradient from the millions of years of magmatism and heat from magma accumulation below allowed these pockets of magma to survive in a more liquid state. Zircons may have crystallized in the mid crust after the hornblendes.

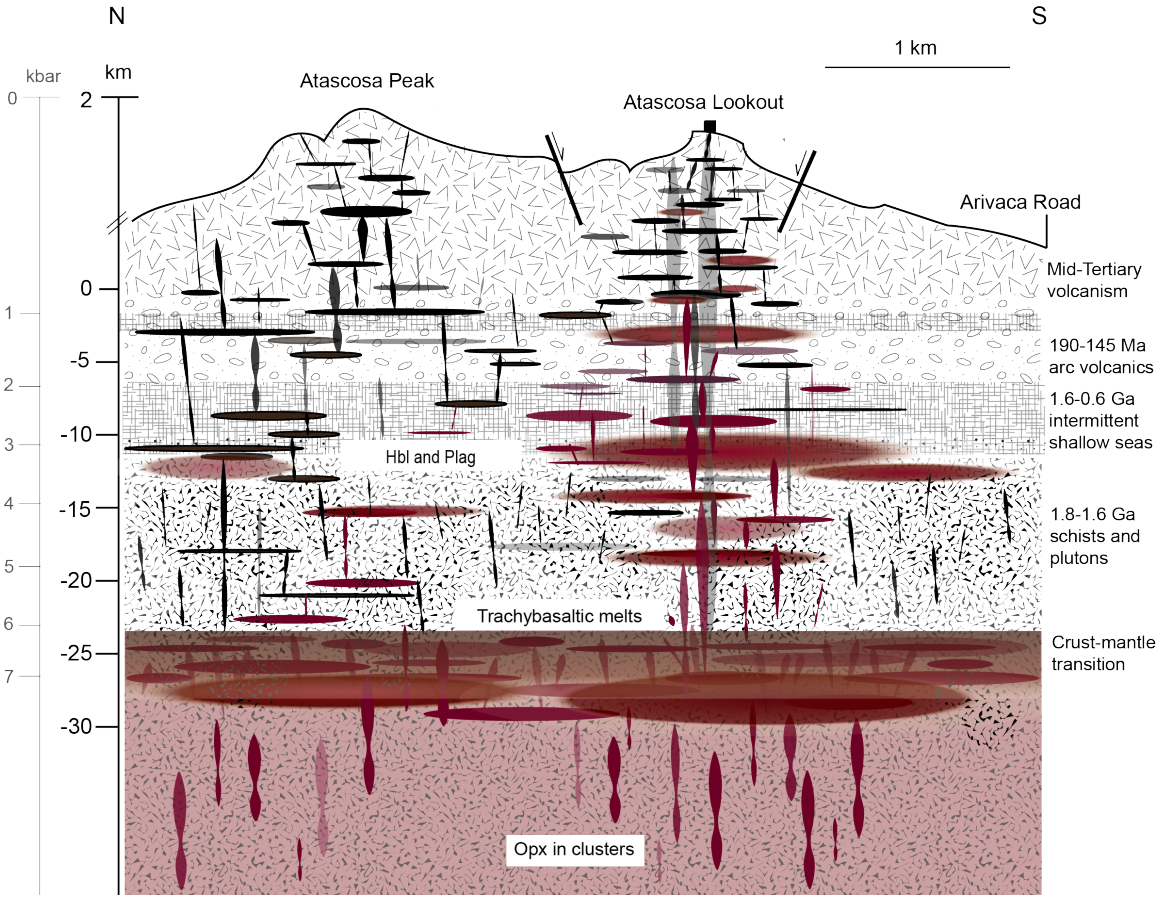

Figure 16. Transcrustal magma plumbing system producing the Atascosa Lookout lava flow. A schematic interpretation of geology, thermobarometry, textural, geochemical data showing multiple levels of mush regions, old magmatic intrusions and the estimated path producing the eruption of the lava flow.

CHAPTER 6

CONCLUSIONS AND FUTURE WORK

6.1 Conclusions

The Atascosa Lookout lava flow records part of the complex history of a magma system that produced explosive and effusive eruptions over four million years. The minerals of the lava flow have textures and compositions suggesting mixing of different magma batches, although the isotopic similarity of crystals in each component (groundmass, enclave, magma envelope) and the similar trace elements patterns suggest that the crystals formed in related magmas that may be partial melts of similar source rocks. The stratified magma chamber model of Seaman (2000) was one of several possible scenarios that could fit the textural and compositional data. However, recent studies show it is possible for batches of magmas to equilibrate across a range of crustal levels and to be tapped in a single eruption. The thermobarometry and the zircon ages suggests that the lava flow sourced crystal components from various levels of the crust and the magma was able to ascend rapidly within an extensional setting.

6.2 Future Work

The Atascosa Lookout Lava flow is a complicated flow that provides abundant opportunity to learn more about its history. The abundant zircons found in this study could be geochemically analyzed in future work in order to use the Ti-in-zircon thermometer for additional temperature constraints and insights into the thermal evolution of the magmatic system. Rather than the theoretical zircon saturation temperature, the Ti-in-zircon thermometer can be used to estimate the temperature of the magma at the time of zircon crystallization (Siégal et al 2018). A spread in zircon

temperatures could confirm that the zircons are antecrysts, sourced from older magmatism within the system. The U-Pb dating indicates there are autocrystic zircons present (their ages are close to time of eruption) therefore Ti-in-zircon temperatures could reveal temperature of crystallization or temperature variations in the magma chambers over time with additional zircon ages. Additionally, identifying antecrystic and inherited zircon can be done by obtaining more zircon ages and comparing them with the independently determined eruption age. Caricchi et al. (2014) have demonstrated that zircon age populations vary predictably as a function of magma flux and the volume of the magma body, therefore thermal modeling using zircon ages may provide additional constraints on the thermal history of the Atascosa Lookout lava flow.

Amphibole reaction rim mineralogy may be a promising tool to distinguish between heating and decompression as the cause of the reaction rims. Decompression experiments produce rims with only orthopyroxene, regardless of the duration of the experiment while short heating events should only produce rims with clinopyroxene (REF). Further electron microprobe analyses on the hornblende rims could test this and try to determine the eruption trigger of the Atascosa Lookout lava flow.

Additional traverses of single crystals of pyroxenes could help strengthen the thermobarometry calculations of this study and find the true range of crystallization temperatures and pressures as well as detailed histories of growth. Future traverses of orthopyroxene should be broken into smaller steps to see if there are other elements that show significant zoning and if the equilibrium melt changes. Traverses of clinopyroxenes in the groundmass and crystal clusters should be made and the equilibrium melts compared to see how they compare. If there are Cr-rich rims enclosed by Cr-poor outer

rims that could be a record of final magma decompression and surface crystallization, in which case published clinopyroxene growth rates ($\sim 10^{-8}$) could be used to calculate ascent rates (Ubide & Kamber, 2018).

Further investigation into the radial clinopyroxenes including additional examples from more thin sections, thermobarometry and trace elements may provide information on a mixing event and possible eruption trigger.

Armienti et al. (2013) developed a new method to estimate magma ascent rates using the well-studied Mt Etna. The method, which has its greatest applicability to the deep levels of magma systems, utilizes pressure-temperature estimates for magmatic crystals and crystal growth rates obtained from crystal size distributions (CSD). Melt inclusions are often used to assess and ascent rates but it appears that melt inclusions commonly just sample shallow depths of magma storage zones (Armienti et al., 2013). Future studies that obtained water contents from clinopyroxene compositions and crystal size distribution of the Atascosa Lookout lava flow could use this method to estimate ascent rates.

Finally, determining the timing of the variety of plagioclase textures would help complete the understanding of the petrogenesis of the lava flow. This could be accomplished through U-series ages, crystal growth estimates, and size distribution and thermobarometry (Cooper & Kent, 2014). U-series ages would provide the absolute time crystals have existed while crystal growth and size would constrain time of crystal growth. The difference of these two times would be the time the crystals were stored in the crust before eruption.

APPENDIX A

CLINOPYROXENE THERMOBAROMETRY

A.1 Equilibrium tests for the clinopyroxene traverse. The observed and predicted components do not all fall on the one to one line for the a) groundmass b) enclaves and c) magma envelopes and therefore are not used for any thermobarometric calculations for this clinopyroxene. Graphs of pressure calculated from several different barometers with two estimates for the equilibrium liquid are shown below with corresponding equilibrium tests.

a) groundmass

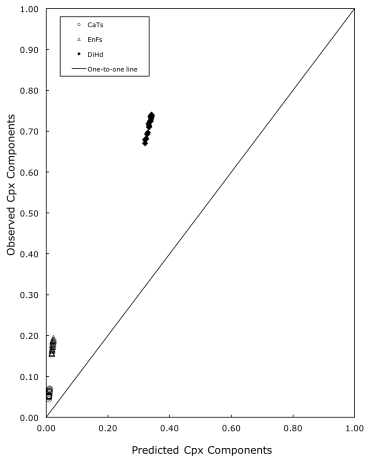

b) enclaves

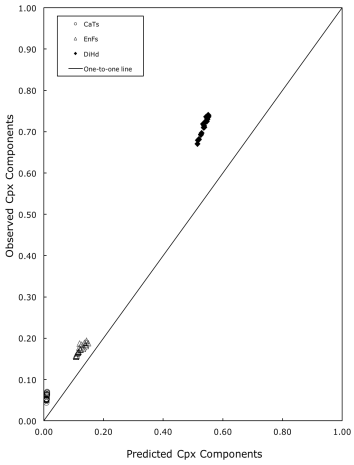

c) magma envelopes

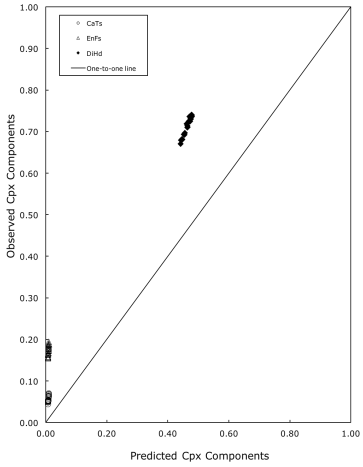

d) estimate 1

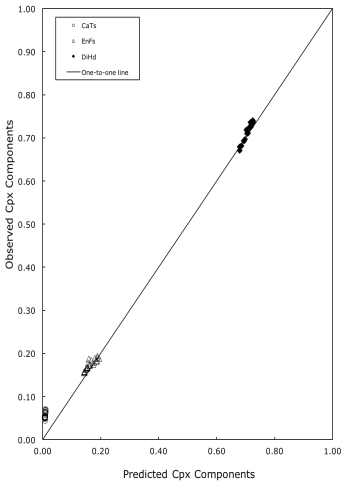

e) estimate 2

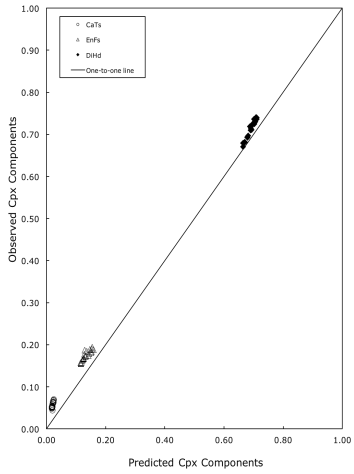

Table A.1 Pressure and temperature calculations for the clinopyroxene traverse. Estimated equilibrium melt compositions 1 and 3 (shaded rows) were used based off where along the traverse the KD(Fe-Mg) ~0.27 ± 0.03. Calculations based on the mineral-melt equilibrium are shown against calculations based on only the clinopyroxene composition.

	Based on cpx and melt				Based on cpx compositions only			
Distance from core	Eqn 30 P(kbar) ± 3.6	Eqn 31 P(kbar) ± 2.9	Eqn 33 T(C) ± 45	Eqn 34 T(C) Sat. ± 45	Eqn 32a P(kbar) ± 3.1	Eqn 32b P(kbar) ± 2.6	Eqn 32c P(kbar) ± 5	Eqn 32d T(C) ± 58
0	5.7	4.1	1211	1180	5.3	4.7	8.1	1193
4	5.4	3.7	1209	1176	4.9	4.3	7.6	1193
7	5.5	4.2	1206	1178	5.1	4.4	8.5	1192
11	5.4	4.0	1205	1176	5.1	4.4	8.6	1189
15	5.4	4.0	1204	1176	5.0	4.3	8.5	1189
18	5.3	4.1	1203	1176	4.8	4.1	8.5	1190
22	5.5	4.3	1204	1179	4.9	4.3	8.6	1192
26	5.6	6.4	1144	1205	4.9	4.3	8.3	1190
29	5.8	6.6	1149	1206	5.8	4.8	4.0	1198
33	6.5	4.6	1205	1194	5.3	4.7	9.3	1201
37	6.2	4.3	1204	1190	5.3	4.5	9.4	1197
40	6.1	4.1	1208	1188	6.1	5.2	10.2	1184
44	6.6	4.7	1214	1194	6.6	5.4	11.6	1187
48	6.8	4.8	1217	1196	6.7	5.5	11.4	1191
51	7.2	5.2	1219	1199	7.0	5.8	12.4	1191
55	7.2	5.3	1220	1199	7.3	5.9	13.0	1184
59	7.2	5.3	1219	1200	7.1	5.8	12.5	1189
63	6.7	4.9	1212	1195	6.5	5.4	11.6	1188
66	6.8	4.9	1213	1196	6.5	5.4	11.6	1187
70	6.2	4.3	1206	1190	5.7	4.8	10.0	1187
74	5.7	3.9	1200	1186	5.2	4.5	9.2	1186
78	5.6	3.6	1202	1141	5.4	4.5	9.0	1183
82	6.7	4.8	1213	1140	6.5	5.4	11.6	1187
86	6.3	4.4	1209	1140	6.2	5.0	11.1	1182
89	5.6	3.7	1200	1141	5.4	4.5	9.4	1183
93	6.4	4.5	1211	1140	6.3	5.1	11.2	1185
27	5.9	4.1	1204	1141	5.8	4.8	10.4	1181
101	7.2	4.7	1229	1140	7.6	6.5	10.9	1186
105	6.6	4.7	1213	1140	6.7	5.4	11.9	1187
109	6.4	4.6	1213	1140	6.7	5.3	12.0	1190

112	4.6	3.0	1202	1168	4.6	3.7	7.2	1185
116	5.2	3.7	1207	1174	5.2	4.3	8.4	1187
120	5.3	3.7	1209	1175	5.2	4.2	8.4	1190
124	5.3	3.7	1206	1175	5.0	4.1	8.3	1190
128	5.5	4.0	1207	1177	4.9	4.2	8.2	1190
132	4.7	3.4	1199	1169	5.0	4.0	8.5	1174
135	6.5	4.3	1212	1140	5.8	4.9	9.6	1198
139	6.3	4.1	1214	1140	6.2	5.1	9.8	1190
143	6.3	4.1	1212	1140	5.8	4.9	9.3	1195
147	6.4	4.3	1211	1140	5.8	4.9	9.5	1196
151	6.5	4.4	1212	1140	5.9	4.9	10.0	1198
155	6.4	4.3	1215	1140	6.6	5.3	11.0	1189
158	6.6	4.6	1215	1140	6.7	5.5	11.5	1191
162	6.6	4.8	1213	1140	6.6	5.3	12.0	1188
166	7.1	5.2	1217	1140	6.9	5.7	12.3	1194
170	5.7	3.9	1199	1141	5.3	4.6	9.1	1186
173	5.3	4.0	1201	1176	4.6	4.2	7.8	1186
177	5.8	4.5	1207	1181	5.3	4.6	8.8	1186
181	5.3	4.0	1202	1176	4.7	4.2	8.1	1184
184	5.3	3.9	1205	1176	5.0	4.4	8.0	1182
188	5.4	3.9	1209	1176	5.7	5.0	8.6	1171
191	5.0	3.7	1199	1174	4.4	4.0	7.5	1183
195	5.2	4.0	1198	1176	4.1	3.8	7.4	1186
199	5.5	4.2	1201	1178	4.5	4.1	7.8	1188
202	5.3	4.0	1199	1176	4.4	4.0	7.8	1182
206	5.6	4.4	1201	1180	4.5	4.2	8.0	1186

APPENDIX B

ORTHOPYROXENE THERMOBAROMETRY

Table B.1 Orthopyroxene Thermobarometry Calculations with 0 wt% H2O

	Thermometers		Barometers (use 28a as input for T)			Test for
	Putirka (2008) RiMG		Putirka (2008) RiMG			Equilibrium
	Eqn. 28a	Eqn. 28b	Eqn 29a	Eqn 29b	Eqn 29c	KD(Fe-Mg)
	T(C) ± 41	Sat. T(C)	P(GPa) ± 3	P(GPa) ± 3	P(GPa)	0.29±0.06
Traverse 7	1354	1396	1.4	1.5	1.4	0.291
rim?	1321	1378	1.3	--	1.2	0.288
	1335	1378	1.3	1.3	1.2	0.288
	1433	1444	1.4	1.7	2.0	0.296
	1383	1421	1.4	1.6	1.6	0.296
	1393	1421	1.5	1.7	1.6	0.270
	1384	1421	1.3	1.5	1.4	0.282
	1434	1443	1.5	1.7	1.8	0.277
	1414	1436	1.5	1.7	1.8	0.284
core?	1496	1450	1.6	2.1	2.5	0.282
Traverse 10	1352	1396	1.3	1.4	1.4	0.295
rim?	1334	1378	1.3	1.3	1.3	0.295
	1333	1378	1.2	1.0	1.1	0.290
	1425	1444	1.4	--	1.7	0.289
	1382	1421	1.3	1.1	1.4	0.289
	1379	1421	1.3	--	1.4	0.294
	1385	1421	1.3	1.3	1.4	0.285
	1432	1443	1.6	1.8	1.9	0.300
	1422	1436	1.4	1.7	1.6	0.305
core?	1484	1450	1.4	--	2.1	0.286
Traverse 16	1354	1396	1.4	1.5	1.4	0.299
rim?	1321	1378	1.3	--	1.2	0.275
	1335	1378	1.3	1.3	1.2	0.297
	1433	1444	1.4	1.7	2.0	0.300
	1383	1421	1.4	1.6	1.6	0.299
	1393	1421	1.5	1.7	1.6	0.294
	1384	1421	1.3	1.5	1.4	0.295
	1434	1443	1.5	1.7	1.8	0.290
	1414	1436	1.5	1.7	1.8	0.300
core?	1496	1450	1.6	2.1	2.5	0.292

Table B.2 Orthopyroxene Thermobarometry Calculations with 3 wt% H2O

	Thermometers		Barometers (use 28a as input for T)		
	Putirka (2008) RiMG		Putirka (2008) RiMG		
	Eqn. 28a	Eqn. 28b	Eqn 29a	Eqn 29b	Eqn 29c
	T(C) ± 41	Sat. T(C)	P(GPa) ± 3	P(GPa) ± 3	P(GPa)
Traverse 7	1289	1323	1.5	1.3	1.0
rim?	1276	1305	1.4	1.3	0.9
	1280	1305	1.5	1.4	1.0
recharge?	1362	1372	1.6	1.5	1.4
	1315	1347	1.4	1.4	1.1
	1323	1347	1.5	--	0.9
	1320	1347	1.3	1.2	0.9
	1358	1370	1.5	--	1.2
	1346	1363	1.4	1.4	1.1
core?	1413	1379	1.5	1.7	1.6
Traverse 10	1289	1323	1.4	1.4	1.0
rim?	1273	1305	1.4	1.3	0.9
	1272	1305	1.3	1.0	0.7
recharge?	1356	1372	1.5	--	1.2
	1316	1347	1.4	1.1	1.0
	1314	1347	1.4	--	1.0
	1319	1347	1.4	1.3	0.9
	1362	1370	1.7	1.7	1.3
	1353	1363	1.5	1.6	1.1
core?	1409	1379	1.5	--	1.5
Traverse 16	1291	1323	1.5	1.5	1.0
rim?	1261	1305	1.4	--	0.9
	1274	1305	1.5	1.3	0.9
recharge?	1363	1372	1.5	1.7	1.4
	1317	1347	1.5	1.5	1.1
	1326	1347	1.6	1.6	1.2
	1318	1347	1.4	1.5	1.0
	1364	1370	1.6	1.6	1.3
	1345	1363	1.6	1.7	1.3
core?	1419	1379	1.7	2.0	1.9

Table B.3 Orthopyroxene estimated equilibrium melt composition for thermobarometry calculations. Melt was estimated from the KD values and the Rhodes's diagram.

SiO_2	TiO_2	Al_2O_3	FeOt	MnO	MgO	CaO	Na_2O	K_2O	Cr_2O_3
43.25	0.68	9.66	20.68	0.28	12.33	11.13	0.95	0.5	0.43

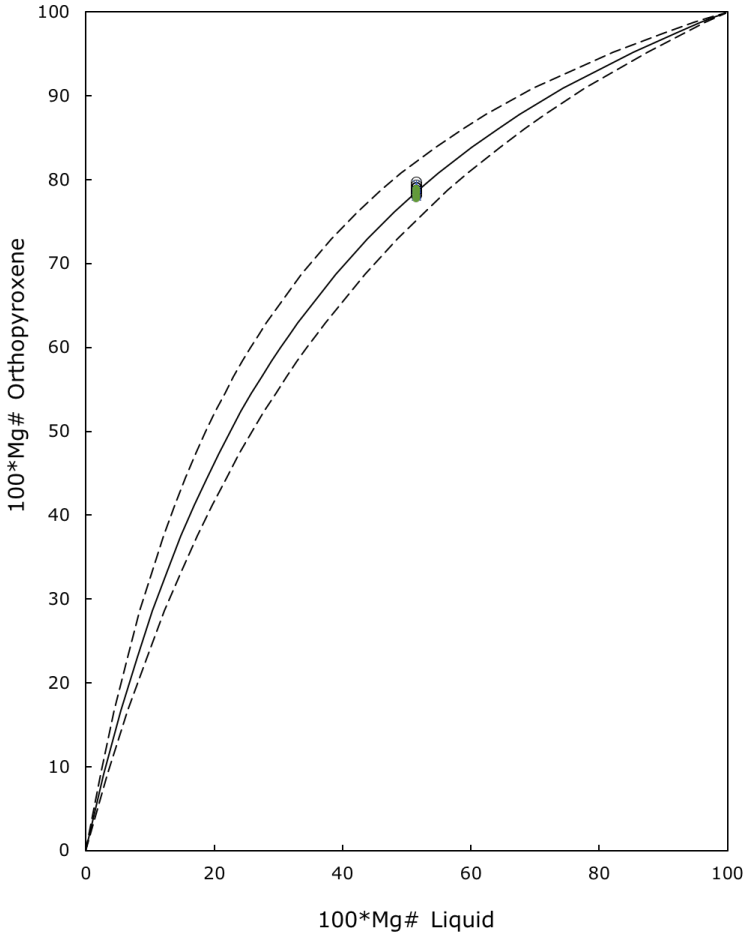

Figure B.1 Rhodes's diagram for all three orthopyroxene traverses.

Table B.4 Electron microprobe analyses of orthopyroxene crystals in a crystal cluster.

Traverse 7										
Distance	0	19	38	56	75	4	113	11	10	169
SiO2	54.12	54.24	56.75	54.15	54.05	55.73	55.1	53.85	55.35	55.4
TiO2	0.25	0.23	0.24	0.26	0.25	0.19	0.2	0.21	0.17	0.2
Al2O3	2.44	2.46	2.64	2.35	2.22	1.32	1.54	1.78	1.44	1.56
FeOt	13.84	13.68	14.04	14.03	13.96	13.46	13.62	13.61	13.72	13.62
MnO	0.35	0.35	0.36	0.38	0.35	0.38	0.35	0.41	0.35	0.34
MgO	28.32	28.35	29.07	28.29	28.1	29.66	28.81	29.32	28.83	28.78
CaO	1.48	1.44	1.5	1.58	1.51	1.56	1.56	1.56	1.63	1.47
Na2O	0.05	0.03	0.05	0.05	0.03	0.05	0.02	0.04	0.02	0.03
K2O	0	0	0	0	0	0	0	0	0	0
NiO	0	0	0	0	0	0	0	0	0	0
Cr2O3	0.37	0.36	0.34	0.34	0.28	0.16	0.2	0.15	0.16	0.22
Total	101.45	101.35	105.03	101.69	100.97	102.77	101.57	101.41	101.84	101.73
FeO	11.99	12.17	13.76	11.91	12.3	11.32	12.26	9.73	12.39	12.77
Fe2O3	2.08	1.7	0.32	2.38	1.86	2.4	1.53	4.36	1.49	0.96
Mg#	81	81	79	81	80	82	81	84	81	80
Traverse 10										
Distance	0	44	88	132	176	220	264	308	352	396
SiO2	53.76	54.21	54.91	52.41	54.81	53.7	55.7	54.23	56.15	55.32
TiO2	0.26	0.24	0.2	0.17	0.2	0.17	0.2	0.18	0.17	0.15
Al2O3	2.9	2.74	1.74	1.59	1.69	1.69	1.63	1.99	1.3	1.29
FeOt	13.92	13.99	13.91	13.77	13.87	13.79	13.87	13.65	13.64	13.83
MnO	0.36	0.34	0.36	0.36	0.39	0.33	0.34	0.35	0.35	0.38
MgO	28.18	28.27	28.56	28.38	28.65	28.01	29.03	27.13	26.68	28.85
CaO	1.47	1.44	1.57	1.52	1.56	1.64	1.58	1.61	1.62	1.64
Na2O	0.03	0.04	0.03	0.04	0.03	0.04	0.03	0.08	0.02	0.03
K2O	0	0	0	0.01	0	0	0	0.02	0	0
NiO	0	0	0	0	0	0	0	0	0	0
Cr2O3	0.44	0.45	0.29	0.26	0.24	0.26	0.22	0.26	0.17	0.17
Total	101.58	101.92	101.75	98.99	101.65	99.89	102.77	99.5	100.1	101.86
FeO	11.9	12.28	12.41	9.74	12.09	11.8	12.53	13.65	13.64	12.23
Fe2O3	2.27	1.92	1.68	4.53	2	2.24	1.5	0	0	1.8
Mg#	81	80	80	84	81	81	81	78	78	81

Traverse 16

Distance	0	22	45	67	89	112	134	156	179	201
SiO2	54.87	49.43	54.63	53.42	54.2	55.98	54.81	55.22	54.6	56.41
TiO2	0.25	0.27	0.21	0.25	0.25	0.24	0.2	0.22	0.25	0.23
Al2O3	2.82	2.72	2.32	2.64	2.62	2.53	1.92	1.93	2.67	2.73
FeOt	14.06	13.62	13.92	13.92	13.97	13.81	13.84	13.68	13.98	13.90
MnO	0.36	0.32	0.35	0.33	0.35	0.33	0.37	0.32	0.35	0.34
MgO	28.04	29.59	27.9	27.67	27.85	28	27.98	28.16	27.77	28.39
CaO	1.48	1.5	1.58	1.58	1.52	1.59	1.5	1.54	1.54	1.48
Na2O	0.04	0.05	0.05	0.03	0.04	0.04	0.03	0.05	0.04	0.04
K2O	0	0	0	0	0	0	0	0	0	0
NiO	0	0	0	0	0	0	0	0	0	0
Cr2O3	0.44	0.45	0.39	0.44	0.43	0.38	0.32	0.31	0.42	0.39
Total	102.42	99.15	101.46	100.47	101.37	102.9	101.03	101.46	101.69	103.92
FeO	13.42	4.11	13.15	12.3	12.88	13.81	13.42	13.47	13.49	13.9
Fe2O3	0.72	10.69	0.86	1.82	1.23	0	0.47	0.24	0.55	0
Mg#	79	93	79	80	79	78	79	79	79	78

FeO=x(Fe2O3t), where x is 0.89
Mg-number is 100Mg / (Mg + Fe)

APPENDIX C

PLAGIOCLASE THERMOBAROMETRY

Table C.1 Plagioclase crystallization temperatures and pressures

	Nominal Equilibrium Melt	$KD_{(Ab-An)}$	Eqn (24a) T(C) ± 36	Eqn (26) T(C) Sat. ± 37	Eqn 25a P(kbar) ± 2.5	Depth (km)
1	Groundmass (0% H2O)	0.13	1041	1032	7.7	28.5
	Groundmass (0.5% H2O)	0.13	1026	1018	7.2	26.6
	130 (1.5% H2O) – Grove & Juster (1989)	0.31	1044	1066	2.0	7.4
	129 (1.5% H2O) – Grove & Juster (1989)	0.33	1049	1071	2.1	7.8
	Enclave (1% H2O)	0.18	1037	1045	2.9	10.7
	Enclave (1.5% H2O)	0.18	1022	1030	2.4	8.9
	Enclave (2% H2O)	0.18	1007	1016	1.8	6.7
	Enclave (2.5% H2O)	0.18	992	1002	1.3	4.8
2	Groundmass (0% H2O)	0.09	1050	1032	5.7	21.2
	Groundmass (0.5% H2O)	0.09	1034	1018	5.3	19.6
	Enclave (0% H2O)	0.13	1078	1075	2.1	7.6
	Enclave (0.5% H2O)	0.13	1062	1060	1.6	5.7
	Enclave (1% H2O)	0.13	1046	1045	1.1	3.9
3	Groundmass (0% H2O)	0.12	1040	1032	6.9	25.5
	Groundmass (0.5% H2O)	0.12	1025	1018	6.4	23.7
	130 (1.5% H2O) – Grove & Juster (1989)	0.29	1043	1066	1.2	4.4
	129 (1.5% H2O) – Grove & Juster (1989)	0.31	1048	1071	1.3	4.8
	Enclave (1% H2O)	0.17	1036	1045	2.1	7.8
	Enclave (1.5% H2O)	0.17	1021	1030	1.6	5.8
	Enclave (2% H2O)	0.17	1006	1016	1.1	3.9
4	Enclave (1% H2O)	0.21	1029	1045	3.6	13.5
	Enclave (2% H2O)	0.21	999	1016	2.5	9.3
	Enclave (2.5% H2O)	0.21	984	1002	2.0	7.3
	Enclave (3% H2O)	0.21	970	988	1.4	5.3
5	Whole rock 1 (0% H2O)	0.15	1096	1080	5.8	21.4
	Whole rock 1 (1% H2O)	0.15	1063	1050	4.7	17.3
	Whole rock 2 (0% H2O)	0.14	1090	1074	6.2	23.1
	Whole rock 2 (1% H2O)	0.14	1057	1044	5.2	19.1
6	Magma envelope (0% H2O)	0.11	1054	1060	12.2	45.1
	130 (1.5% H2O) – Grove & Juster (1989)	0.34	1039	1066	2.2	8.1
	129 (1.5% H2O) – Grove & Juster (1989)	0.36	1044	1071	2.3	8.5
	Enclaves (0.5% H2O)	0.19	1048	1060	3.7	13.7
	Whole rock 2 (0.6 % H2O)	0.27	1048	1056	8.8	32.6

Table C.1 (cont.) Plagioclase crystallization temperatures and pressures

	Nominal Equilibrium Melt	$KD_{(Ab-An)}$	Eqn (24a) T(C) ± 36	Eqn (26) T(C) Sat. ± 37	Eqn 25a P(kbar) ± 2.5	Depth (km)
7	CPX estimate 1 (0% H2O)	0.18	1098	1105	2.8	10.4
	CPX estimate 1 (1% H2O)	0.18	1065	1073	1.7	6.3
	142A (0% H2O) -Rutherford et al. (1985)	0.12	1101	1101	5.1	18.9
	142A (1% H2O) -Rutherford et al. (1985)	0.12	1068	1069	4.1	15.2

Nominal pressure of equilibration of 1.65 kbar used for calculations for whole rock, groundmass, envelopes and enclaves
Plagioclase thermobarometry equations from Putirka (2008)

Table C.2 Feldspar compositions used for thermobarometry calculations

	wt. %	SiO2	Al2O3	FeOt	CaO	Na2O	K2O
1	Groundmass phenocryst	57.85	27.20	0.47	9.01	6.05	0.64
2	Groundmass phenocryst	55.76	28.22	0.66	10.61	5.2	0.43
3	Laths in groundmass	56.75	27.2	0.56	9.93	6.22	0.36
4	Plagioclase in enclaves	59.02	26.37	0.53	7.99	6.32	0.46
5	Center of plagioclase in cluster & honeycomb	52.85	29.19	0.58	12.2	4.7	0.39
6	Honeycomb rim	56.66	27.2	0.45	9.01	6.56	0.49
7	Dusty Core	55.18	28.8	0.21	10.8	5.43	0.33

Feldspar compositions from Seaman (2000)

APPENDIX D

ZIRCON SATURATION CALCULATIONS

Table D.1 Zircon saturation thermometry compositional inputs and parameters.

Wt%	Whole Rock Analyses**			Average Groundmass**
SiO2	62.23	60.94	60.21	67.76
Al2O3	16.81	16.51	16.62	18.26
TiO2	0.88	0.86	0.91	0.41
FeO*	5.39	5.37	5.83	0.66
MgO	1.69	1.93	2.61	0.2
CaO	4.4	4.38	5.1	3.06
Na2O	3.69	3.8	3.84	6.41
K2O	3.9	4.43	3.73	3.46
ppm Zr in rock	456.8	459	485.4	467
M	1.87	2.02	2.10	1.71
G	5.16	4.85	4.41	7.97

*FeO calculated by Fe_2O_3 x 0.9

The Zr (ppm) of the groundmass is the average of the three whole rock analyses

** Analyses from Seaman (2000)

Table D.2 Zircon saturation calculations. Variable concentrations of zircon in the groundmass was used to evaluate the possible temperature range.

Zr (ppm)	Temperature	
800	invalid	Temperature would be too high for zircon to crystallize
700	904	
600	877	
500	844	
400	829	
300	753	Below crystallization temperature for the groundmass

*FeO calculated by Fe_2O_3 x 0.9

** Analyses from Seaman (2000)

APPENDIX E

PARTITION COEFFICIENTS

Table E.1 Partition coefficients. Coefficients obtained from the online GERM database for calculations of parental melts for amphibole and clinopyroxene. Composition of melt used in partition coefficient study chosen to match results from thermobarometry equilibrium tests.

Trace Element	Amphibole Luhr et al. 1984 Trachyandesite	Clinopyroxene Hauri et al. 1994 Basalt
Cs	-	0.0058
Rb	-	-
Ba	0.15	0.0058
Th	0.054	0.014
U	0.05	0.0127
Nb	-	0.0081
Ta	0.56	-
La	0.54	0.0515
Ce	0.98	0.108
Pb	0.6	0.0102
Pr	-	-
Sr	-	0.157
Nd	2.1	0.277
Zr	-	0.195
Hf	0.76	0.223
Sm	2.99	0.462
Eu	2.88	0.458
Ti	-	0.451
Gd	-	-
Tb	4.8	-
Dy	4.3	0.711
Li	-	-
Y	-	-
Ho	-	-
Er	-	0.66
Tm	-	-
Yb	2.29	0.633
Lu	2.3	0.623
V	-	1.81
Co	22	-
Zn	-	-

BIBLIOGRAPHY

Andersen, D.J., Lindsley, D., Davidson, P.M. (1993) A PASCAL program to assess equilibria among Fe–Mg–Mn–Ti-oxides, pyroxenes, olivine, and quartz. *Comput. Geosci.* 19, 1333–1350.

Anderson, J.L., Smith, D.R. (1995) The effects of temperature and fO2 on the Al-in-hornblende barometer. *Am. Mineral.* 80, 549–559.

Anderson, J., Barth, A., Wooden, J., & Mazdab, F. (2008). Thermometers and thermobarometers in granitic systems. *Reviews in Mineralogy and Geochemistry, 69*, 121-142.

Annen, C., Blundy, J.D., Sparks, R.S.J. (2006) The Genesis of Intermediate and Silicic Magmas in Deep Crustal Hot Zones. *Journal of Petrology*, 47, 505-539.

Annen, C. (2009) From plutons to magma chambers: thermal constraints on the accumulation of eruptible silicic magma in the upper crust. *Earth Planet. Sci. Lett.* 284 (3-4), 409-416.

Annen, C., Blundy, DJ., Leuthold, J., Sparks, RSJ. (2015) Construction and evolution of igneous bodies: towards an integrated perspective of crustal magmatism. *Lithos* 230, 206-221.

Armienti, P., Perilnelli, C. & Putirka, K.D. (2013) A new model to estimate deep-level magma ascent rates, with applications to Mt. Etna (Sicily, Italy). *Journal of Petrology* 54, 795-813.

Armstrong, R.L. and Ward, P. (1991) Evolving Geographic Patterns of Cenozoic Magmatism in the North American Cordilleran: The Temporal and Spatial Association of Magmatism and Metamorphic Core Complexes, *Journal of Geophysical Research* 96, 13201-13224.

Bergantz, G.W., Schleicher, J.M. & Burgisser, A. (2015) Open-system dynamics and mixing in magma mushes. *Nature Geoscience* 8, 793-797.

Blundy, J., Cashman, K.V. (2008) Petrologic reconstruction of magmatic system variables and processes. *Rev Mineral Geochem* 69, 179–239.

Boehnke, P., Watson, E. B., Trail, D., Harrison, T. M. & Schmitt, A.K. (2013) Zircon saturation re-visited. *Chemical Geology* 351, 324-334.

Bryan, S.E., Ferrari, L., Reiners, P.W., Allen, C.M., Petrone, C.M., Ramos-Rosique, A., Campbell, I.H. (2008) New insights into crustal contributions to large-volume rhyolite generation in the Mid-Tertiary Sierra Madre Occidental province, Mexico, revealed by U–Pb geochronology. *J. Petrol.* 49 (1), 47.

Caricchi, L., Simpson, G. & Schaltegger, U. (2014) Zircons reveal magma fluxes in the Earth's crust. *Nature* 511, 457-461.

Cashman, K. & Giordano, G. (2014) Review: Calderas and magma reservoirs. *Journal of Volcanology and Geothermal Research* 288, 28-45.

Cassidy, M., Edmonds, M., Watt, S. F. L., Palmer, M. R., Gernon, T. M. (2015) Origin of Basalts by Hybridization in Andesite-dominated Arcs. *Journal of Petrology*, 56, 325–346.

Charlier, B.L.A., Wilson, C.J.N., Lowenstern, J.B., Blake, S., Van Calsteren, P.W., Davidson, J.P. (2005) Magma generation at a large, hyperactive silicic volcano (Taupo, New Zealand) revealed by U–Th and U–Pb systematics in zircons. *J. Petrol.* 46 (1), 3–32.

Christiansen, R. L. & Lipman, P. W. (1972). Cenozoic volcanism and plate-tectonic evolution of the western United States. II. Late Cenozoic. *Philosophical Transactions of the Royal Society of London*, Series A 271, 249-284.

Copeland, P., Currie, C., Lawton, T., Murphy, M. (2017) Location, Location, Location: The variable lifespan of the Laramide Orogeny. *Geology* 45, 223-226.

Costa, F. & Morgan, D. (2011) in Timescales of Magmatic Processes: From Core to Atmosphere. Eds Bonaccorso, A., Turner, S. P. & Van Orman, J. A., Blackwell Publishing Ltd., Chichester, West Sussex, UK.

De Angelis, S.H., Larsen, J., Coombs, M., Dunn, A. & Hayden, L. (2015). Amphibole reaction rims as a record of pre-eruptive magmatic heating: An experimental approach. *Earth and Planetary Science Letters* 426, 235-245.

Elston, W. E. (1984). Subduction of young oceanic lithosphere and extensional orogeny in southwestern North America during mid-Tertiary time. *Tectonics* 3, 229-250.

Gans, P. B., Mahood, G. A. & Schermer, E. 1989; Synextensional magmatism in the Basin and Range province: a case study from the eastern Grest Basin. *Geological Society of America, Special Paper* 233, 53 pp.

Geiger, H., Barker, A. and Troll, V. (2016) Locating the depth of magma supply for volcanic eruptions, insights from Mt. Cameroon. *Scientific Reports* 6, 33629.

Gervasoni, F., Klemme, S., Rocha-Junior, E. R. V., & Berndt, J. (2016) Zircon saturation in silicate melts: a new and improved model for aluminous and alkaline melts. *Contrib. Mineral Petrol.* 171, 21.

Giardina, Jr., S. and Conley, J.N., 1978, Thermal Gradient Anomalies, Southern Arizona. Arizona Geological Survey, Oil & Gas (OG) -27, 49 p., scale 1:1,382,400, 3 sheets.

Goodwin, E.B. and McCarthy, J. (1990) Composition of the Lower Crust in West Central Arizona from Three-Component Seismic Data. *Journal of Geophysical Research* 95, 20097-20109.

Hammarstrom, J.M., Zen, E.A. (1986) Aluminium in hornblende: an empirical igneous geobarometer. *Am. Mineral.* 71, 1297–1313.

Hanchar, J.M., Watson, E.B. (2003) Zircon saturation thermometry. *Rev. Mineral. Geochem.* 53 (1), 89.

Hauri, E.H., Wagner, T.P. and Grove, T.L. (1994). Experimental and natural partitioning of Th, U, Pb and other trace elements between garnet, clinopyroxene and basaltic melts. *Chemical Geology 117*, 149-166.

Humphreys, E.D., Dueker, K.G. (1994) Physical state of the western U.S. upper mantle. *Journal of Geophysical Research* 99, 9635-9650.

Johnson, M.C., Rutherford, M.J. (1989) Experimental calibration of the aluminium-in-hornblende geobarometer with application to Long Valley caldera (California) volcanic rocks. *Geology* 17, 837–841.

Karakas, O. & Dufek, J. (2015) Melt evolution and residence in extending crust: Thermal modeling of the crust and crustal magmas. *Earth and Planetary Science Letters* 425, 131-144.

Lachenbruch, A. H., and Sass, J. H. (1977) Heat flow in the United States and the thermal regime of the crust, in The Earth's Crust: Its Nature and Physical Properties Geophys Monogr. Ser. vol. 20, edited by J. G. Heacock, p p. 626-675, AGU, Washington D, .C.

Lachenbruch, A.H., Sass, J. H., Morgan, P. (1994) Thermal regime of the southern Basin and Range Province: 2. Implications of heat flow for regional extension and metamorphic core complexes. *Journal of Geophysical Research* 99, 22121-22133.

Leeman, W. P. & Fitton, J. G. (1989). Magmatism associated with lithospheric extension: introduction. *Journal of Geophysical Research* 94, 7682-7684.

Lipman, P.W. & Glazner, A.F. (1991) Introduction to the Middle Tertiary Cordilleran volcanism: magma sources and relations to regional tectonic. *Journal of Geophysical Research* 96, 13193-13199.

Lofgren, G. (1971) Spherulitic textures in glassy and crystalline rocks. *Journal of Geophysical Research*, 76 pp. 5635-5648

Luhr, J.F., Carmichael, I.S.E. and Varekamp, J.C. (1984). The 1982 eruptions of El Chichon volcano, Chiapas, Mexico: mineralogy and petrology of the anhydrite-bearing pumices. *Journal of Volcanology and Geothermal Research* 23, 69-108.

Lustrino, M. & Anderson, D. L. (2015) The mantle isotopic printer: Basic mantle plume geochemistry for seismologists and geodynamicists. In: Foulger,G.R., Lustrino, M., King, S.D. (eds) *The Interdisciplinary Earth: A Volume in Honor of Don L. Anderson. Geological Society of America, Special Paper* 514, 257–279.

Marks, M., Halama, R., Wenzel, T. & Markl, G. (2004) Trace element variations in clinopyroxene and amphibole to peralkaline syenites and granites: implications for mineral-melt trace element partitioning. *Chemical Geology* 211, 185-215.

McGuire, A. (1994) Southern Basin and Range provine crust-mantle boundary: Evidence from gabbroic xenoliths, Wikieup, Arizona. *Journal of Geophysical Research* 99, 24263-24273.

McPhie, J., Doyle, M., Allen, R., & University of Tasmania. Centre for Ore Deposit and Exploration Studies. (1993). *Volcanic textures : A guide to the interpretation of textures in volcanic rocks*. Hobart, Tas.: Centre for Ore Deposit and Exploration Studies, University of Tasmania.

Menard, T., de Saint-Blanquat, M. & Annen, C. (2011) Emplacement of magma pulses and growth of magma bodies. *Tectonophysics* 500, 1-2.

Mollo, S., Blundy, J. D., Iezzi, G., Scarlato, P. & Langone, A. (2013) The partitioning of trace elements between clinopyroxene and trachybasaltic melt during rapid cooling and crystal growth. *Contrib. Mineral. Petrol.* 166, 1633–1654.

Nelson, F.J. (1963) The geology of the Pena Blanca and Walker Canyon areas, Santa Crux County, Arizona. MSc. Thesis, University of Arizona, Tucson, 82 pp.

Orlando, A., D'Orazio, M., Armienti, P. & Borrini, D. (2008) Experimental determination of plagioclase and clinopyroxene crystal growth rates in an anhydrous trachybasalt from Mt. Etna (Italy). Eur. J. Mineral. 20, 653–664.

Parsons, T., The Basin and Range Province, K.H. Olsen (Ed.), Continental Rifts Evolution, Structure, Tectonics, New York (1995), pp. 277-324

Paterson, S. and Ducea, M. (2015) Arc Magmatic Tempos: Gathering the Evidence. *Elements* 11, 91-98.

Paterson, S., Okaya, D., Memeti, V., Economos, R. & Miller, R. (2011) Magma addition and flux calculations of incrementally construction magma chambers in continental margin arcs: combined field, geochronologic, and thermal modeling studies. *Geosphere* 7, 1439-1468.

Putirka, K. (1997) Magma transport at Hawaii: inferences based on igneous thermobarometry. *Geology* 25, 69-72.

Putirka, K., Mikaelian, H., Ryerson, F. & Shaw, H. (2003) New clinopyroxene-liquid thermobarometers for mafic, evolved and volatile bearing lava compositions with applications to lavas from Tibet and the Snake River Plain, Idaho. *American Mineralogist* 88, 1542-1554.

Putirka, K. (2008) Thermometers and barometers for volcanic systems. *Reviews in Mineralogy and Geochemistry* 69, 61-120.

Putirka, K. (2017). Down the crater: Where magmas are stored and why they erupt. *Elements* 13, 11-16.

Reynolds, S.J., Welty, J. W., & Spencer, J.E., (1986) Volcanic History of Arizona, Arizona Bureau of Geology and Mineral Technology Fieldnotes, v. 16

Ridolfi, F., Renzulli, A., Puerini, M. (2010) Stability and chemical equilibrium of amphibole in calc-alkaline magmas: an overview, new thermobarometric formulations and application to subduction-related volcanoes. *Contrib Mineral Petrol* 160, 45–66

Ridolfi, F., Renzulli, A. (2012) Calcic amphiboles in calc-alkaline and alkaline magmas: thermobarometric and chemometric empirical equations valid up to 1130 °C and 2.2 GPa. *Contrib Mineral Petrol* 163, 877–895.

Seaman, S., Scherer, E. and Standish, J. (1995) Multistage magma mingling and the origin of flow banding in the Aliso lava dome, Tumacacori Mountains, southern Arizona. *Journal of Geophysical Research* 100, 8381-8398.

Seaman, S. (2000) Crystal clusters, feldspar glomerocrysts and magma envelopes in the Atascosa Lookout Lava Flow, Southern Arizona, USA: Recorders of Magmatic Events. *Journal of Petrology* 41, 693-716.

Siégal, C., Bryan, S.E., Allen, C.M. & Gust, D.A. (2018) Use and abuse of zircon-based thermometers: A critical review and a recommended approach to identify antecrystic zircons. *Earth-Science Reviews* 176, 87-116.

Schmidt, M.W. (1992) Amphibole composition in tonalite as a function of pressure; an experimental calibration of the Al-in-hornblende barometer. *Contrib. Mineral. Petrol.* 110, 304–310.

Spencer, J.E., Richard, S.M., Reynolds, S.J., Miller, R.J., Shafiqullah, M., et al. (1995) Spatial and temporal relationships between mid-Tertiary magmatism and extension in southwestern Arizona. *J. Geophys. Res.* 100:10,321–10,351

Streck, M. (2008) Mineral textures and zoning as evidence for open system processes. *Reviews in Mineralogy and Geochemistry* 69, 595-622.

Ubide, T. and Kamber, B. S. (2018) Volcanic crystals as time capsules of eruption history. *Nature Communications* 9, 326.

Watson, E.B., Harrison, T.M. (1983) Zircon saturation revisited: temperature and composition effects in a variety of crustal magma types. *Earth Planet. Sci. Lett.* 64 (2), 295–304.

Watson, E.B. (1996) Dissolution, growth and survival of zircons during crustal fusion:kinetic principles, geological models and implications for isotopic inheritance. *Geol.Soc. Am. Spec. Pap.* 315, 43–56.

Webb, B. P., and Coryell, K. C. (1954) Preliminary regional mapping in the Ruby Quadrangle Arizona, U.S. Atomic Energy Commission Washington D.C., Tech. Rep. RME-2009, 12 pp.

Winter, J. (2010) Principles of Igneous and Metamorphic Petrology. New Jersey. Prentice Hall.